

# RANS simulations of neutral atmospheric boundary layer flow over complex terrain with comparisons to field measurements

Yi Han  | Michael Karl Stoellinger

Department of Mechanical Engineering,  
 University of Wyoming, Laramie, Wyoming

**Correspondence**

Yi Han, Department of Mechanical  
 Engineering, University of Wyoming, Laramie,  
 Wyoming, 82072.  
 Email: [yhan@uwyo.edu](mailto:yhan@uwyo.edu)

## Abstract

Micro-scale Reynolds-averaged Navier-Stokes (RANS) simulations of the neutral atmospheric boundary layer (ABL) over complex terrain and a comparison of the results with conditionally averaged met-tower data are presented. A robust conditional sampling procedure for the meteorological tower (met-tower) data to identify near-neutral conditions based on a criterion for the turbulence intensity is developed. The conditionally averaged wind data on 14 met-towers are used for the model validation. The ABL flow simulations are conducted over complex terrain which includes a prominent hill using the OpenFOAM-based simulator for on/offshore wind farm applications (SOWFA) with the  $k-\epsilon$  and the SST  $k-\omega$  turbulence models. The discretization of the production term in the transport equation for the turbulent kinetic energy (TKE) is modified to greatly reduce the commonly observed nonphysical near surface TKE peak. The driving inflow is generated through an iterative approach using a precursor method to reproduce the measured wind statistics at the reference tower. Both of the RANS models are able to capture the flow behavior windward of the hill. The SST  $k-\omega$  model predicts more intense flow separation than the  $k-\epsilon$  model downstream of the steepest sections of the hill. The wind statistics predicted at the location of the met-towers by both of the RANS models are fairly consistent. Overall, the comparisons of the direction, mean, and standard deviation of the wind between the simulations and the tower data show reasonable agreement except for the differences of the mean wind speeds at four met-towers located closer to the main ridge of the hill in a region of strong terrain variations.

## KEYWORDS

atmospheric boundary layer, complex terrain, field measurements,  $k-\epsilon$  model, neutral stability, Reynolds-averaged Navier-Stokes (RANS) simulations, SST  $k-\omega$  model

## 1 | INTRODUCTION

Nowadays, the focus of wind energy project innovation is shifting from individual turbine performance to overall wind plant performance characteristics, resulting in a significant drop in the wind electricity generation costs.<sup>1</sup> For example, the levelized cost of electricity (LCOE) from wind in good (wind power class IV) to excellent (class V) resource sites in the United States had fallen from \$71/megawatt-hour (MWh) in the year 2008 to \$45/MWh in 2013, a decrease of more than one-third during these five years. On-shore commercial wind farms are often located in complex

The peer review history for this article is available at <https://publons.com/publon/10.1002/we.2412>

terrain with hills, ridges, and even mountain slopes. The interaction of these complicated landforms with the atmospheric boundary layer (ABL) turbulent flow may greatly affect both the character of the large scale flow over wind farms and the local flow features such as flow acceleration, separation, and recirculation. Therefore, a detailed wind resource analysis for a prospective wind site is important for the wind engineers to accurately predict the power output from the entire wind plants.

The most direct way to obtain wind resource information for a prospective wind farm is to conduct field measurements with meteorological towers (met-towers). The monitoring duration for the met-tower observation typically lasts for at least 1 year to obtain a sufficient number of samples so that reliable statistical analysis of diurnal and seasonal variability of the wind can be determined.<sup>2</sup> Due to cost limitations, the met-towers are usually sparsely distributed across the wind farm site, and thus, they only provide a highly localized assessment of the wind conditions. Extrapolation of the wind conditions from the tower locations to other regions of the wind farm is difficult in complex terrain. To overcome these limitations, micro-scale computational fluid dynamics (CFD) modeling of ABL flow is becoming more ubiquitous. It extends the measured wind distributions from met-tower positions to any other positions especially the prospective turbine sites, and thereby, one can obtain a high-resolution atmospheric flow field with detailed insight into the local flow characteristics.<sup>3</sup>

Another important application of micro-scale CFD ABL simulations is to provide realistic turbulent inflow for high-fidelity blade-resolved wind farm simulations.<sup>4-6</sup> In this simulation approach, the blade boundary layers are typically modeled with the Detached Eddy Simulation (DES) method,<sup>7</sup> and the atmospheric boundary layer is modeled with the Large Eddy Simulation (LES) method. Both methods require a sufficiently fine mesh resolution in order to capture the relevant atmospheric scales that influence the blade and wake aerodynamics. The purpose of the micro-scale CFD modeling of the ABL with a spatial resolution on the order of 10 to  $10^2$  m is to bridge the scale gap between meso-scale weather prediction models<sup>8,9</sup> with a resolution on the order of  $10^3$  m and the wind farm CFD simulations with a fine resolution from 10 m down to  $10^{-4}$  m.

Micro-scale CFD simulations of the ABL utilize either the Reynolds-averaged Navier-Stokes (RANS) or the LES approach. The RANS approach is based on the ensemble averaged governing equations and thus the effects of all the scales of turbulent motion need to be modeled by a turbulence model. The LES approach, which is based on solving the spatially filtered governing equations, resolves the large scale turbulent motion directly and only models the small scale (subgrid-scale, SGS) motions. Therefore, LES generally provides higher fidelity solutions but is at least one order of magnitude more computationally expensive than RANS.<sup>10</sup> Due to the reduced computational cost, the most common CFD approach used in the wind energy industry is the RANS approach with two-equation turbulence models among which the standard  $k-\epsilon$  model<sup>11</sup> is the most popular one.<sup>12,13</sup> However, it has been noted that the near-surface performance of the  $k-\epsilon$  model is somehow unsatisfactory for capturing the proper behavior of turbulent boundary layers with adverse pressure gradients up to separation.<sup>14,15</sup> The  $k-\omega$  based Shear Stress Transport (SST) model<sup>16</sup> is developed to effectively combine the robust formulation of the original  $k-\omega$  model<sup>17</sup> in the near-surface region and the free-stream independence of the  $k-\epsilon$  model in the region far from the wall. The SST  $k-\omega$  model which is originally used for aeronautics applications has been also adopted in wind energy engineering due to the more accurate prediction of the flows around bluff bodies immersed in the ABL and the ABL with pressure induced separation.<sup>18-20</sup>

Along with the increased use of micro-scale CFD simulations for wind energy applications comes the need for providing more evidence of the accuracy of the simulation results. However, recent efforts to validate CFD simulation results of ABL flows have struggled mainly due to the lack of sufficient field measurements. The CFD model results have been validated in the past through wind tunnel measurements performed at laboratory scales.<sup>21,22</sup> These experiments are performed over simplified terrain forms whose geometrical properties are rarely found in the real world. Several full-scale field experiments<sup>23-25</sup> have been conducted to validate the numerical approach and turbulence models at atmospheric scales and real terrain. However, these field campaigns have a limited number of measurement locations and are not intended to become actual wind farm sites.

In the present work, the wind characteristics over complex terrain are predicted by RANS based micro-scale turbulence models (i.e.,  $k-\epsilon$  and SST  $k-\omega$  models) and the simulation results are compared with field measurements using 14 met-towers. The complex terrain is located within the Chokecherry and Sierra Madre (CCSM) wind farm site which encompasses about 500 km<sup>2</sup> of rugged and diverse terrain in south-central Wyoming. The CCSM wind energy project is the largest proposed commercial wind generation facility in North America.<sup>26</sup> Wind data have been recorded on the met-towers for periods ranging from 2 to 7 years which is long enough to obtain the regional wind characteristics with a high level of confidence. The simulation of neutral ABL flow over part of the CCSM wind site is performed using the OpenFOAM-based simulator for on/offshore wind farm applications (SOWFA).<sup>27</sup> SOWFA is an open source software containing incompressible ABL flow solvers for wind simulation through flat and complex terrain. So far, the SOWFA solver has mostly been used for LES of ABL flow over flat terrain and idealized sinusoidal curve topography with varying atmospheric stabilities.<sup>28-30</sup> In this study, the SOWFA solver is extended by implementing new boundary conditions as needed for flow over real complex terrain.

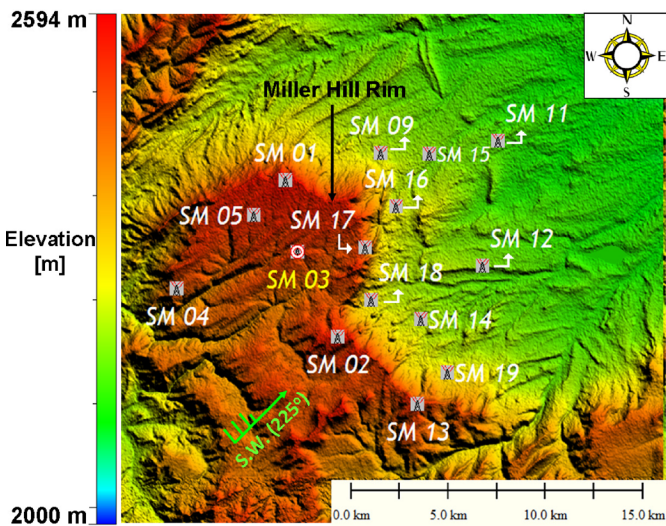
The paper is organized as follows. A conditional sampling procedure is developed and applied to the wind data from the met-tower measurements in Section 2 to create a canonical near neutral case for comparison with micro-scale CFD simulation results. In Section 3, the methodology of the neutral ABL flow simulation over complex terrain is described including the adopted RANS turbulence models, inflow generation, boundary conditions, and numerical implementations. In Section 4, the inflow statistics, mesh independence, and domain height influence of RANS-ABL simulation are analyzed. The simulated flow fields are displayed in terms of contour plots of important wind variables. In Section 5, the wind statistics at the location of each met-tower predicted from simulations with both  $k-\epsilon$  and SST  $k-\omega$  models are quantitatively analyzed in comparison with the conditional averaged met-tower data. Concluding remarks and suggestions are provided in the final section.

## 2 | WIND DATA ACQUISITION AND ANALYSIS

### 2.1 | Site description and met-towers information

The terrain of interest for this work is within the Sierra Madre (SM) wind site which is in the south-west part of the CCSM site. The SM wind site is located approximately between  $41^{\circ} 27'1.9''$  N and  $41^{\circ} 35'25.0''$  N in latitude and between  $107^{\circ} 13'1.0''$  W and  $107^{\circ} 24'53.0''$  W in longitude. The wind power resource of this area in terms of annual average wind speed measured at 50 m ranges from "outstanding" (class VI) to "superb" (class VII) levels.<sup>31</sup> A prominent topographical feature named "Miller Hill" with an approximate 400-m elevation difference traverses longitudinally across the wind site. The long-term regional climate records<sup>32</sup> indicate that the annual prevailing wind of this area comes from the south-west (SW) direction which is between  $213.75^{\circ}$  and  $236.25^{\circ}$  in azimuth angle in a classical wind rose diagram with 16 cardinal directions.<sup>33</sup> The topography of the SM site obtained from the 1-arc-second (30-m horizontal resolution) Shuttle Radar Topography Mission (SRTM) data set<sup>34</sup> is shown in Figure 1A. By analyzing the SRTM data around Miller Hill, the steepest region in this area is found to have a slope of approximately 45%. A photo of the Miller Hill ridge near the steepest region is shown in Figure 1B. It is found that the surface of this area can be treated as fairly level uncut long grass with few low height trees growing only on the lee side of the hill, which would imply an aerodynamic surface roughness height  $z_0$  between  $10^{-1}$  and  $10^{-2}$  m.<sup>35</sup>

Fourteen met-towers had been deployed within the SM site around the rim of Miller Hill to assess the regional wind resources. Each met-tower is equipped with cup anemometers at three above ground levels (AGL) ranging from 30 to 60 m (except met-tower SM 05 with anemometers installed between 40- and 80-m AGLs) to capture the wind variation with height. The anemometers capture the wind speed and direction with a frequency of 1 Hz simultaneously. The data are averaged and recorded over 10-minute interval following IEC standards<sup>36</sup> in terms of mean magnitudes and standard deviations of horizontal wind speed and direction. The detailed preprocessing of the raw data such as removing the tower shadowing effects from the original data sets can be found in the research work by Matthew Welch and Jonathan Naughton.<sup>37</sup> Since only one thermometer is installed near the surface of each met-tower, the vertical temperature profiles are not available. In order to estimate the atmospheric stability without multipoint vertical temperature information, one could adopt weather prediction models such as the Weather Research and Forecasting (WRF) Model.<sup>38,39</sup> These weather prediction models would be required to run on a relatively coarse grid resolution (typically larger than 1 km) over the region of interest for several years of simulation time to match the investigation time period of the met-towers. An alternative approach to infer the local atmospheric stability is to adopt a purely wind statistic based criterion which uses the wind data collected at the met-towers. In the present study, the latter approach is adopted due to the long data records available from a large number of met-towers. The investigation on using the wind statistic based stability assessment presented below might also be relevant for wind site developers since multipoint temperature measurements are typically not installed on met-towers for the wind resource evaluation due to high equipment cost.<sup>2</sup>



(A) 1-arc-second SRTM topography of the SM wind site. Met-towers locations and prevailing wind direction are shown.



(B) Photograph of the Miller Hill Rim near met-tower SM 01

**FIGURE 1** Overview of the Sierra Madre (SM) wind energy project site [Colour figure can be viewed at [wileyonlinelibrary.com](http://wileyonlinelibrary.com)]

## 2.2 | Wind statistics-based atmospheric stability classification

To estimate the regional atmospheric stability using only horizontal wind speed data measured with cup anemometers, the criterion developed by Wharton and Lundquist<sup>40</sup> is used. In their work, the horizontal turbulence intensity (TI) at 80-m AGL (which is usually the wind turbine hub height) is used as the stability parameter. The horizontal TI for the cup anemometers is determined by

$$TI_{Qcup} = \frac{\sigma_Q}{Q}, \quad (1)$$

where  $Q$  and  $\sigma_Q$  are the 10-minute averaged horizontal mean velocity magnitude and standard deviation, respectively. The  $TI_{Qcup}$  thresholds for five stability classes (including strongly stable, stable, near-neutral, convective, and strongly convective) have been proposed by Wharton and Lundquist.<sup>40</sup> In their work, the cup anemometers were installed on a met-tower located near a wind farm in grassland with elevation variations of less than 100 m. The threshold for  $TI_{Qcup}$  at 80-m AGL for near-neutral atmospheric stability was found to be  $9\% < TI_{Qcup} < 12\%$ . This neutral stability criterion is applicable for the current SM site as long as the chosen reference met-tower is located among a fairly flat terrain and not close to the main ridge of the Miller hill, such that the elevation variation and surface roughness are comparable with those in the Wharton and Lundquist's study.<sup>40</sup> However, due to the fact that the highest AGL of the cup anemometers on most of the met-towers within the SM site is 57 m, the neutral stability threshold for  $TI_{Qcup}$  needs to be scaled from 80- to 57-m AGL.

For ideal flat terrain with neutrally stratified atmosphere, the vertical profile of  $TI_{Qcup}$  up to about 100-m AGL is commonly represented by the logarithmic law<sup>41</sup> as

$$TI_{Qcup}(z) = \frac{\sigma_Q(z)}{Q(z)} = \sigma_Q(z) \frac{\kappa}{u_* \ln(z/z_0)} = \kappa \frac{A_Q}{\ln(z/z_0)} = \frac{1}{\ln(z/z_0)}, \quad (2)$$

where  $A_Q$  is the ratio of  $\sigma_Q$  to  $u_*$ , experimentally found to be around 2.5 so that  $\kappa A_Q$  is about 1.0.<sup>42</sup> Here the dimensionless von Karman constant  $\kappa$  is chosen to be 0.42, and  $u_*$  is the friction velocity. Therefore, from Equation (2)  $TI_{Qcup}(z_2)$  can be estimated based on the given value of  $TI_{Qcup}(z_1)$  as<sup>43</sup>

$$TI_{Qcup}(z_2) = TI_{Qcup}(z_1) \frac{\ln(z_1/z_0)}{\ln(z_2/z_0)}, \quad (3)$$

where  $TI_{Qcup}(z_1)$  is regarded as the documented neutral stability threshold at  $z_1 = 80$  m and  $TI_{Qcup}(z_2)$  is the estimated neutral stability threshold at the measuring height  $z_2 = 57$  m on the reference tower within SM site. The specific value of  $z_0$  is determined iteratively within the range between  $10^{-1}$  and  $10^{-2}$  m, which is based on the surface roughness of the terrain type mentioned before. The iteration process (see Section 3.4 for details) converges to  $z_0 = 0.035$  m leading to a good agreement of the wind statistics between simulation and measurements at the reference tower. The neutral stability threshold for  $TI_{Qcup}$  at 57-m AGL based on this  $z_0$  is then computed by Equation (3) to be  $9.41\% < TI_{Qcup} < 12.55\%$ .

## 2.3 | Conditional sampling of the reference met-tower data

### 2.3.1 | Selection of the reference tower and terrain ruggedness analysis

The reference tower within the SM site should be selected such that the wind statistic based neutral stability criterion can be adopted. The met-tower SM 03 is selected as the reference tower due to the fact that it is located on relatively flat terrain (with maximum elevation variations of around 100 m) over an area of approximately 4 km × 4 km in the upstream region at the plateau of Miller hill. The tower SM 03 also has the longest data recording history (8 y) among all the met-towers. The tower SM 05 could be another possible choice for the main reference met-tower, but it is not chosen since it is located closer (~2 km) to the main ridge of Miller hill and it has a much shorter recording time than SM 03. However, SM 05 can still be used as an alternative reference tower to verify the robustness of the stability criterion, which will be shown in Section 5.3.

With the reference met-tower being selected as SM 03, the complexity of the SM site can be quantified by using the ruggedness index (RIX) as suggested by Mortensen and Peterson.<sup>44</sup> The recommended calculation radius  $r = 3.5$  km, critical slope  $\theta_c = 30\%$  and the number of radii  $N_r = 12$  are used to conduct the terrain ruggedness analysis. The orographic performance indicator  $\Delta RIX$  is defined as the difference in the RIX percentage between the predicted and reference tower sites. The maximum difference of  $\Delta RIX$  in the SM site is seen between SM 18 ( $RIX \approx 4.51\%$ ) and SM 03 ( $RIX \approx 2.26\%$ ) as approximately 2.3%, which corresponds to less than 5% of the  $WA^S P^{45}$  wind speed prediction error. It seems adequate to also consider a more local RIX by choosing a calculation radius of  $r = 1$  km and by weighting with the wind rose to account for the prevailing wind direction. With this choice, we find the  $RIX_{SM03} \approx 0\%$  and  $RIX_{SM18} \approx 1\%$ , which indicates that the extrapolation of the wind resource from SM 03 to SM 18 is within a small uncertainty. We also consider two locations on the lee of the steep ridge near SM 13 and SM 01 for which the

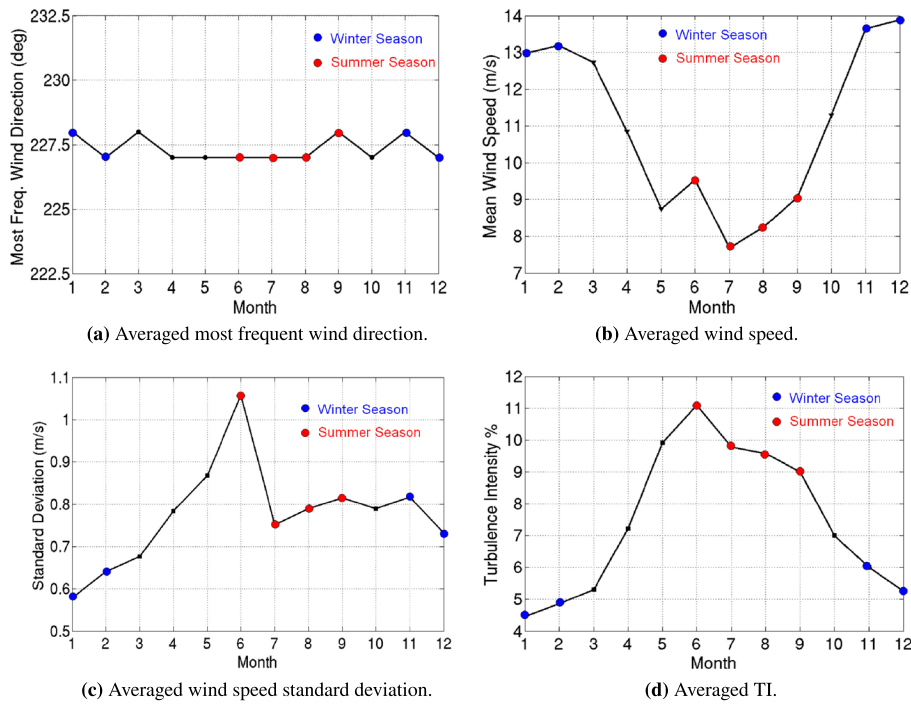


**FIGURE 2** Monthly averaged wind quantities at 57-m AGL on the reference met-tower SM 03 [Colour figure can be viewed at [wileyonlinelibrary.com](http://wileyonlinelibrary.com)]

CFD results (see Figure 15) predict a recirculation region. Indeed, the local  $\Delta RIX$ s with respect to SM 03 are larger than 10% for both locations and thus the RIX method would correctly suggest a large extrapolation error.

### 2.3.2 | Monthly analysis of the reference tower data

The complete wind data set recorded on the reference tower SM 03 at 57-m AGL is denoted by  $R^{57m}$ . An arbitrary sample  $R_i^{57m}$  with index  $i$  consists of a time  $t_i$  (combining the date and time of day), 10-minute averaged wind speed  $Q_i$ , 10-minute averaged standard deviation  $\sigma_{Q,i}$ , and 10-minute averaged direction  $\Phi_i$ . The most frequent wind direction, the averaged values of wind speed, the wind speed standard deviation, and the turbulence intensity of  $R^{57m}$  based on monthly averages are shown in Figure 2. The prevailing (most frequent) wind direction is uniformly around 227.5° throughout a year. The averaged wind speed varies significantly over a year with much higher wind speeds in the winter months (November, December, January, and February) as compared with the lower wind speeds in the summer months (June, July, August, and September). The averaged wind speed standard deviations also change throughout a year with the highest values observed in June and the lowest values observed in January. The TI calculated by Equation (1) combines the statistical moments of averaged wind speed and wind speed standard deviation. It can be seen that higher TI values ( $TI > 9\%$ ) are observed during the summer months than those ( $TI < 6\%$ ) observed during the winter months. This means that a convective ABL (unstable stratification) dominates during the summer season (increased turbulence through buoyant production) while a stable ABL dominates during the winter. Due to the distinct averaged wind speeds, wind speed standard deviations and TI properties of the regional wind resource, a conditional sampling process will be conducted within these two distinct seasons.

### 2.3.3 | Conditional sampling using season, wind speed, and direction

The conditional data sets obtained during summer and winter are termed and defined as  $R_S^{57m}$  and  $R_W^{57m}$ , respectively,

$$R_S^{57m} = \{\forall R_i^{57m} | t_i \in \text{Summer months}\}, \quad (4)$$

$$R_W^{57m} = \{\forall R_i^{57m} | t_i \in \text{Winter months}\}. \quad (5)$$

During the summer, the wind speed and direction sampling condition (denoted by  $\vec{V}$ ) is defined as  $8.59 \text{ m/s} \pm 0.5 \text{ m/s}$  from  $227^\circ \pm 5^\circ$ . The wind direction range is chosen to coincide with the most frequent wind direction with a range of about half of a typical wind sector width. The wind speed range is determined by the mean wind speed of the summer months with a variation of around 5% of the mean value in order

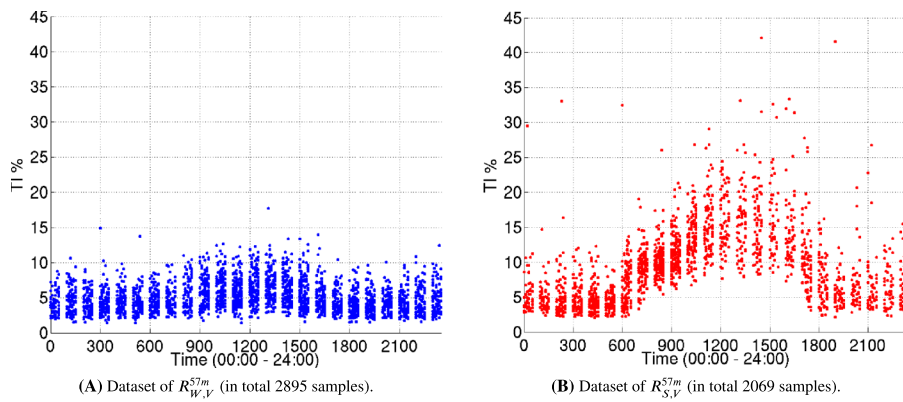


**FIGURE 3** Diurnal distribution of the 10-min averaged TI at 57-m AGL on the reference tower SM 03 over 8 years [Colour figure can be viewed at wileyonlinelibrary.com]

to obtain a sufficient number of samples. The conditional data set obtained by applying the wind speed and direction sampling condition  $\vec{V}$  is termed  $R_{S,\vec{V}}^{57m}$  and defined as

$$R_{S,\vec{V}}^{57m} = \{\forall R_{S,i}^{57m} | 8.09 \text{ m/s} \leq Q_i \leq 9.09 \text{ m/s}; 222^\circ \leq \Phi_i \leq 232^\circ\}. \quad (6)$$

Similarly, the wind speed and direction sampling conditions for winter are  $13.4 \text{ m/s} \pm 0.5 \text{ m/s}$  from  $227.5^\circ \pm 5^\circ$ , and its corresponding conditional data set is termed  $R_{W,\vec{V}}^{57m}$  and defined as

$$R_{W,\vec{V}}^{57m} = \{\forall R_{W,i}^{57m} | 12.9 \text{ m/s} \leq Q_i \leq 13.9 \text{ m/s}; 222.5^\circ \leq \Phi_i \leq 232.5^\circ\}. \quad (7)$$

The diurnal turbulence intensity distributions of  $R_{W,\vec{V}}^{57m}$  and  $R_{S,\vec{V}}^{57m}$  are plotted in Figure 3. For both seasons, the TI follows a diurnal pattern related to the atmospheric stability. During the daytime, the surface heating process resulting from solar irradiation causes an unstable stratification with strong convective mixing and high turbulence levels. The turbulence intensity peaks around noon (between 11:00 and 15:00), which are the warmest hours of the day. During the night-time, the atmosphere tends to be stably stratified due to the surface cooling with a corresponding suppression of turbulence. The typical diurnal pattern of TI is fairly pronounced during the summer including near neutral samples but is far less distinct during the winter. In winter, the TI values of the wind are low enough to fall into the stable categories. Since we are interested in near-neutral conditions for the ABL simulation, only the conditional data set of the summer months  $R_{S,\vec{V}}^{57m}$  will be considered in the subsequent analysis.

### 2.3.4 | Conditional sampling using the neutral stability criterion

A two-step sampling approach is performed on the reference tower data set  $R_{S,\vec{V}}^{57m}$  to obtain wind data with neutral stability. The turbulent intensity threshold  $9.41\% \leq TI_{Qcup} \leq 12.55\%$  defining the neutral condition at 57-m AGL is applied first. The data points marked in black shown in Figure 4A are the samples of  $R_{S,\vec{V}}^{57m}$  satisfying the neutral stability criterion. These samples are thus defined as

$$R_{S,\vec{V},N}^{57m} = \{\forall R_{S,\vec{V},i}^{57m} | 9.41\% \leq TI_{Qcup,i} \leq 12.55\%\}. \quad (8)$$

It can be seen that most of the samples in  $R_{S,\vec{V},N}^{57m}$  are found to be occurring in the morning and late afternoon. However, quite a few samples are observed during the noon-time and night-time. These periods of time are usually associated with convective and stable conditions, respectively. To add more robustness to the stability sampling, a second condition is imposed so that only the samples in  $R_{S,\vec{V},N}^{57m}$  satisfying the neutral TI criterion for at least two consecutive recording times (20 min) will be considered. The data set of these samples are then defined as

$$R_{S,\vec{V},N,\bar{t}}^{57m} = \{\forall R_{S,\vec{V},N,i}^{57m} | t_{i+1} - t_i = 10\text{min} \quad \text{or} \quad t_i - t_{i-1} = 10\text{min}\}. \quad (9)$$

The reason for conducting the second sampling condition is to ensure that the neutral condition lasts over a sustained period of time instead of occurring by chance. The lower panel in Figure 4B shows the outcome of the second sampling step ( $R_{S,\vec{V},N,\bar{t}}^{57m}$  with purple symbols) along with the outcome of the first sampling step ( $R_{S,\vec{V},N}^{57m}$  with black symbols). It can be seen that most of the data collected during the noon and night times are

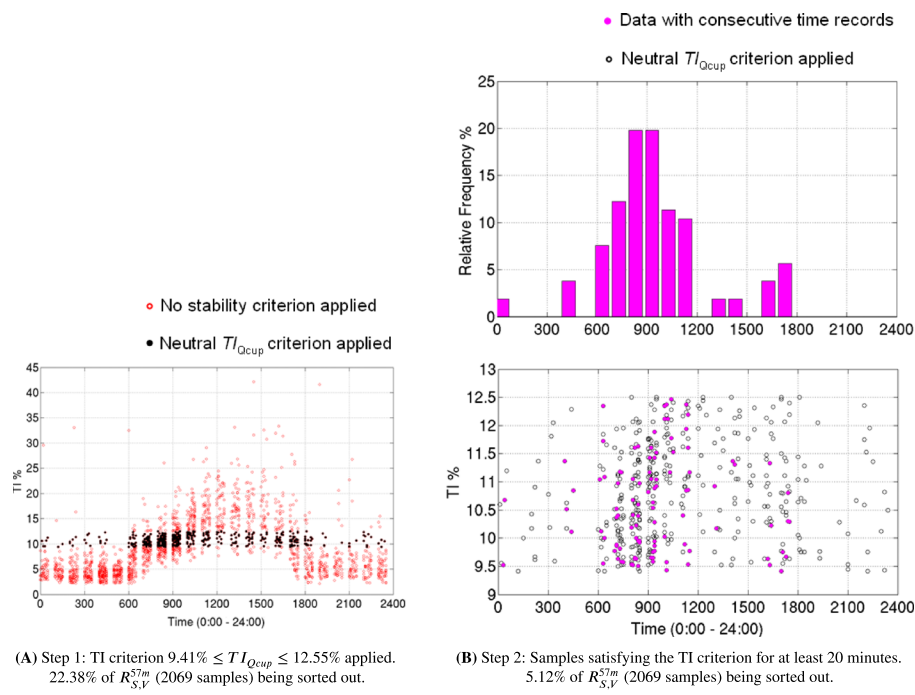


**FIGURE 4** Diurnal distributions of 10-min averaged TI by applying the two-step neutral stability sampling approach [Colour figure can be viewed at [wileyonlinelibrary.com](http://wileyonlinelibrary.com)]

eliminated by the second sampling step. This is further evidenced in the upper panel of Figure 4B where the relative frequency of the neutral data set  $R_{S,V,N,\bar{t}}^{57m}$  over a day is shown. The time stamps of the samples in  $R_{S,V,N,\bar{t}}^{57m}$  are concentrated in the few hours after sunrise (between 07:00 and 11:00) and before sunset (between 16:00 and 17:00), which is consistent with the conventional time periods when a neutral atmosphere is expected to occur.<sup>35,40</sup> Wharton and Lundquist<sup>40</sup> also proposed a second criterion for neutral stability based on the wind shear exponent  $0.1 \leq \alpha \leq 0.2$ . This criterion is less suitable for application in complex terrain<sup>46</sup> and thus was not used in this work. It is nevertheless reassuring that the average wind shear exponent calculated from the conditional samples on SM 03 ( $R_{S,V,N,\bar{t}}^{57m}$ ) falls within the neutral range  $0.1 \leq \alpha_{SM03}=0.13 \leq 0.2$ .

## 2.4 | Conditional averaged results at all met-towers

The conditional wind statistics on all met towers are calculated based on the neutral samples of the reference tower SM 03 assuming that the atmospheric stability does not vary spatially within the SM site. The time stamps  $t_i$  from  $R_{S,V,N,\bar{t}}^{57m}$  are used to sample the data from data sets of the other two AGLs at SM 03 and from the data sets of the three AGLs on all other met-towers. The neutral wind samples collected at 57-m AGL on the non-reference met-tower, e.g., SM 01, according to the time stamps of the data in  $R_{S,V,N,\bar{t}}^{57m}$  are termed as  $M01^{57m}_{S,C,\bar{t}}$ . The conditional averaged wind speed and wind speed standard deviation of all met-towers are computed as arithmetic means over the corresponding data sets. The complete workflow to obtain the conditional averaged wind statistic of all met-towers is shown in Figure 5.

### 2.4.1 | Sample space information on met-towers

The sample space information on each met-tower under the neutral condition is studied first. The percentage of the conditional neutral data is calculated as the ratio of the number of neutral samples to the number of wind samples before applying the neutral stability criterion. For the reference tower SM 03,

$$\text{Neutral percentage} = \frac{N(R_{S,V,N,\bar{t}}^{57m})}{N(R_{S,V}^{57m})} \times 100\%, \quad (10)$$

and for the non reference tower, e.g., SM 01,

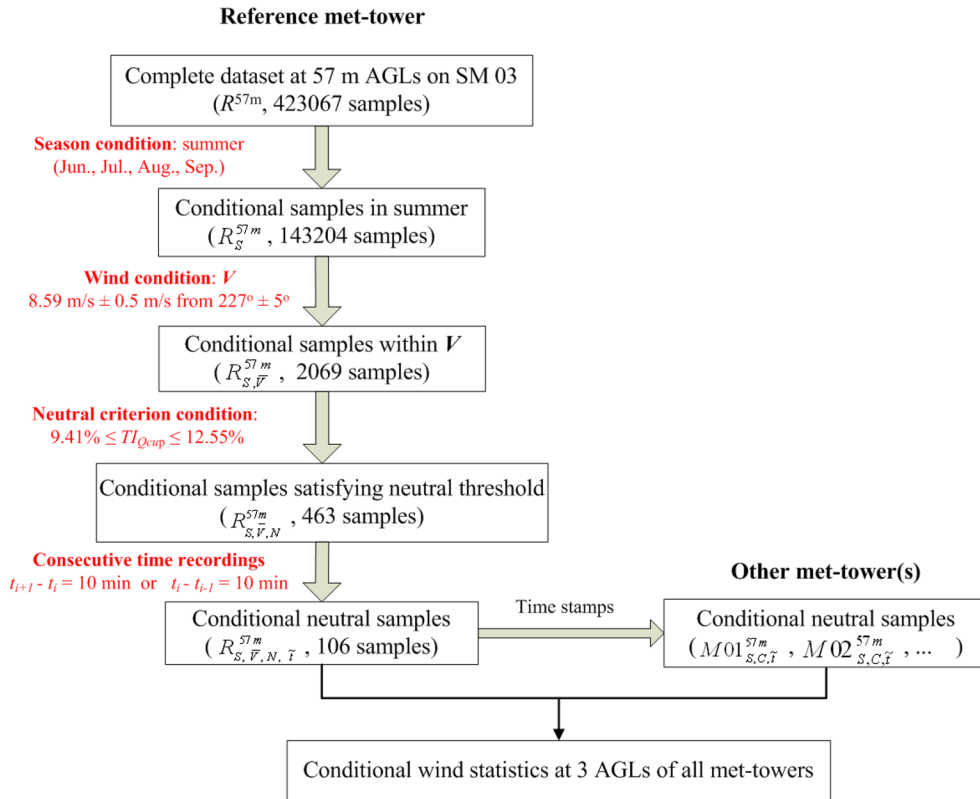


**FIGURE 5** The work flow to create the conditional averaging wind statistics under neutral stability [Colour figure can be viewed at [wileyonlinelibrary.com](http://wileyonlinelibrary.com)]

$$\text{Neutral percentage} = \frac{N(M01_{S,C,t}^{57m})}{N(M01_{S,C}^{57m})} \times 100\%. \quad (11)$$

The number of neutral samples varies according to the data collecting period on each met-tower. The reference met-tower SM 03 has the most samples due to its longest data recording history. Even though the number of the neutral samples at these met-towers is widely distributed over a range between 31 and 106, the percentage values of neutral data are quite similar. Overall, around 5% of the conditional wind data are sampled as having neutral stability on each met-tower.

#### 2.4.2 | Wind rose plots

The wind rose calculated on each met-tower at 57-m AGL are shown in Figure 18 in Section 5.3. It gives a succinct view of how wind speed and direction are typically distributed at each tower location so that the effect of the terrain on the real (measured) flow field can be seen. On the reference tower SM 03, the wind rose has only one concentrated sector for both speed and direction due to the specified sampling condition ( $\vec{V}$ ). The real wind shows obvious variations in both wind speed and direction when passing through the towers (SM 01, 02, 13, and 17) located near the edge of the hill. These variations might be induced by the topographic features located upstream and the elevation gradient of the terrain located behind. The wind roses of the met-towers located behind the main ridge show a similar wind direction as at the reference tower. The wind recovery in the downstream region of the domain will be quantitatively analyzed in the next subsection.

In order to explore the effect of the main ridge on the flow field nearby, the conditional sampling procedures have been reconducted based on a different wind sampling direction ( $\Phi$ ).  $\Phi$  has been changed from SW to 202° ± 5° (within the South-southwest (SSW) sector) and to 248° ± 5° (within the West-southwest (WSW) sector), respectively. It is found that the wind roses (not shown for the sake of brevity) obtained on the met-towers located close to the main ridge always show variations from the sampling wind direction on the reference tower. The most frequent wind sectors obtained on the met-towers located downstream of the main ridge are always the same as the sampling wind direction. This finding indicates that the local topography of the main ridge has a great influence on the wind speed and direction in its neighborhood.

### 2.4.3 | Wind statistics

As the Miller Hill stretches along the cross-stream section of the domain, quantitative data analysis is conducted based on the location of the met-towers relative to the main ridge. For the met-towers (SM 01, 02, 03, 05, 13, and 17) located upstream of the main ridge, the conditional averaged wind speed profiles are computed and shown in Figure 19A marked by blue circles with the corresponding uncertainties. The uncertainty is obtained by calculating the standard deviation of the 10-minute averaged wind speeds. The conditional averaged wind statistics of SM 03 is overlaid on the plots for all the other towers (as blue dashed lines) in order to show the changes of the wind profiles with respect to the reference tower. On the met-towers (SM 01, 02, 13, and 17) located near the rim at the peak region of Mill hill which is about 80 m higher than the upstream terrain, the flow experiences an acceleration (favorable pressure gradient) compared with the flow at SM 03 due to the up-slope of the terrain in between.

The conditional averaged wind speed standard deviation profiles from the met-towers located upstream of the main ridge are shown (blue circles) in Figure 19B. Note that the range of uncertainty here is obtained as the standard deviation of the 10-minute averaged wind speed standard deviation values. It is seen that the wind speed standard deviations on most of the towers (except SM 01) is slightly smaller than that on the reference tower. The levels of uncertainty for the wind speed standard deviations on tower SM 02 are larger than those on other towers. The turbulence intensity profiles at these met tower locations are similar to the standard deviation profiles and are thus not shown. Overall, we find that the met-towers SM 01, 02, 13 and 17, which experience a flow acceleration as compared with SM 03, all have 10-15% lower TI values than SM 03. The reduced TI values are likely caused by the favorable pressure gradient boundary layer conditions on these towers. Such a decrease of the TI in the boundary layer with favorable pressure gradient has been observed in the log-law region of turbulent boundary layers over a smooth wall.<sup>47</sup>

The conditional averaged wind speed profiles of met-towers (SM 09, 11, 12, 14, 15, 16, 18, and 19) located downstream of the main ridge are shown in Figure 20A. The mean wind speed is expected to decrease somewhat in the region just behind the main ridge due to the drastic elevation drop (with adverse pressure gradient), which is similar to a typical back-step flow.<sup>48</sup> However, the mean wind speed profiles on most of the met-towers hardly show any significant changes compared with the flow at the reference tower. This can be explained by the fact that the distances (at least 1 km) between the foot of the hill and these met-towers might be sufficient for the air entertainment from the upper atmosphere to compensate for the mean flow deceleration. The downstream met-towers are not located in regions of boundary layer separation and recirculation. At tower SM 09 the flow even experiences an approximate 15% acceleration compared with the reference tower.

The conditional averaged wind speed standard deviation profiles calculated on the met-towers located downstream of the main ridge are shown in Figure 20B. The averaged values at the met-towers SM 09, 16, 18, and 19 located close to the lee side of the hill increase significantly compared with the values of reference tower. As the flow streams down over relatively flat terrain and reaches the towers SM 11 and 12 located relatively far from the main ridge, the values of wind speed standard deviation seem to relax towards the values of the reference tower. Moreover, the values of turbulence intensity calculated on all downstream tower locations (not shown) for which the boundary layer has experienced an adverse pressure gradient are 15% to 20% larger than those on the reference tower. Increased TI values in adverse pressure gradient boundary layers have also been observed in the research of Harun.<sup>47</sup>

## 3 | MODELING THE ABL FLOW OVER COMPLEX TERRAIN FOR NEUTRAL STABILITY

### 3.1 | Governing equations

The incompressible RANS equations including Coriolis force are adopted to model the neutral ABL flow.<sup>12,13,49,50</sup> The continuity equation for the mean flow is

$$\frac{\partial \bar{u}_i}{\partial x_i} = 0, \quad (12)$$

and the momentum equation for the mean flow is

$$\frac{\partial \bar{u}_i}{\partial t} + \frac{\partial (\bar{u}_j \bar{u}_i)}{\partial x_j} = -\frac{1}{\rho} \frac{\partial \bar{p}_{mod}}{\partial x_i} - \frac{1}{\rho} \frac{\partial p_0(x, y)}{\partial x_i} + v \frac{\partial^2 \bar{u}_i}{\partial x_j \partial x_i} - \frac{1}{\rho} \frac{\partial T_{ij}^d}{\partial x_j} - 2 \varepsilon_{ijk} \Omega_j \bar{u}_k. \quad (13)$$

In these equations, the over line denotes an ensemble averaged quantity,  $\bar{u}_i$  is the averaged velocity field in the Cartesian coordinate direction  $x_i$ ,  $\varepsilon_{ijk}$  is the alternating unit tensor,  $\Omega_j$  is the earth rotation rate vector computed as  $\omega[0, \cos(\phi), \sin(\phi)]$ , where  $\omega=7.27 \times 10^{-5}$  rad/s is the earth rotation rate, and  $\phi=41.51^\circ$  is the average latitude of the wind site. The kinematic viscosity of air is assumed constant at  $v=1 \times 10^{-6}$  m<sup>2</sup>/s and a constant density of  $\rho = 1$  kg/m<sup>3</sup> is adopted. For fully periodic precursor simulations a spatially varying pressure gradient  $\partial p_0(x, y)/\partial x_i$  is used to achieve a

specified horizontal wind vector at a specified height. The deviatoric part of the Reynolds stress tensor is  $T_{ij}^d = T_{ij} - T_{kk}\delta_{ij}/3$  and one-third of the trace of the Reynolds stress tensor is lumped into the pressure term<sup>51</sup> leading to a modified pressure  $\tilde{p}_{mod} = \bar{p} - \rho gh + T_{kk}\delta_{ij}/3$ , where  $\bar{p}$  is the mean dynamic pressure,  $\rho gh$  represents the hydrostatic pressure,  $g=9.81\text{m/s}^2$  is the gravitational constant, and  $h$  is the height above the ground.

### 3.2 | Turbulence modeling

The evolution of the mean velocity  $\bar{u}_i$  is affected by the turbulent motion through the unclosed Reynolds stress  $T_{ij} = \rho \bar{u}_i \bar{u}_j'$ . The Reynolds stress tensor must be parametrized by using a turbulence model as a function of the averaged velocity fields to close the equation system. By adopting the eddy viscosity assumption,<sup>52</sup> the deviatoric part of  $T_{ij}$  is modeled to be proportional to the mean velocity gradients using a turbulent viscosity  $v_T$ :

$$T_{ij}^d = -2\rho v_T \bar{S}_{ij}, \quad (14)$$

where  $\bar{S}_{ij} = \frac{1}{2} \left( \frac{\partial \bar{u}_i}{\partial x_j} + \frac{\partial \bar{u}_j}{\partial x_i} \right)$  is the mean flow strain rate tensor. In this work, we use the  $k-\epsilon$  and the SST  $k-\omega$  models to obtain  $v_T$ . It is important to point out that with the eddy viscosity assumption the final form of the momentum equation that is actually solved numerically reads

$$\frac{\partial \bar{u}_i}{\partial t} + \frac{\partial (\bar{u}_j \bar{u}_i)}{\partial x_j} = -\frac{1}{\rho} \frac{\partial \tilde{p}_{mod}}{\partial x_i} - \frac{1}{\rho} \frac{\partial p_0(x, y)}{\partial x_i} + \frac{\partial}{\partial x_j} \left[ (\nu + v_T) \frac{\partial \bar{u}_i}{\partial x_j} \right] + \frac{\partial v_T \partial \bar{u}_i}{\partial x_j} - 2\varepsilon_{ijk} \Omega_j \bar{u}_k, \quad (15)$$

where the combined molecular and turbulent diffusion is treated implicitly and the term  $\frac{\partial v_T \partial \bar{u}_i}{\partial x_j}$  involving the transpose of the velocity gradient tensor is treated explicitly.

#### 3.2.1 | $k-\epsilon$ model

Applying the dimensional analysis, the kinematic turbulent viscosity can be described as the product of a length scale ( $l=k^{3/2}/\epsilon$ ) with a velocity scale ( $v=k^{1/2}$ ) to yield the well-known  $k-\epsilon$  model<sup>11</sup>:

$$v_T = C_\mu \frac{k^2}{\epsilon}, \quad (16)$$

where  $C_\mu$  is a nondimensional model constant. The standard  $k-\epsilon$  model, which has been widely used in computational wind engineering, solves the following transport equations for  $k$  and  $\epsilon$

$$\frac{\partial k}{\partial t} + \frac{\partial (\bar{u}_j k)}{\partial x_j} = \frac{\partial}{\partial x_j} \left( v_T \frac{\partial k}{\partial x_j} \right) + P_k - \epsilon, \quad (17)$$

$$\frac{\partial \epsilon}{\partial t} + \frac{\partial (\bar{u}_j \epsilon)}{\partial x_j} = \frac{\partial}{\partial x_j} \left( v_T \frac{\partial \epsilon}{\partial x_j} \right) + C_{1\epsilon} \frac{\epsilon}{k} P_k - C_{2\epsilon} \frac{\epsilon^2}{k}, \quad (18)$$

where the production of turbulent kinetic energy (TKE) is

$$P_k = 2v_T \bar{S}_{ij} \bar{S}_{ij}. \quad (19)$$

Equation (16), (17), and (18) contain five adjustable constants which are assigned the standard values  $C_\mu=0.09$ ,  $\sigma_k=1$ ,  $\sigma_\epsilon=1.3$ ,  $C_{1\epsilon}=1.44$  and  $C_{2\epsilon}=1.92$ .

#### 3.2.2 | SST $k-\omega$ model

To express the kinematic turbulent viscosity  $v_T$ , the dissipation rate of turbulence kinetic energy is not the only possible length scale determining variable. The turbulence frequency  $\omega = \epsilon/k$  can be used as an alternative variable, resulting in the length scale as  $l = \sqrt{k}/\omega$ . The kinematic turbulent viscosity can then be obtained from the SST  $k-\omega$  model as<sup>53</sup>

$$v_T = a_1 \frac{k}{\max(a_1 \omega, SF_2)}, \quad (20)$$

where  $a_1$  is a constant taken as 0.31.  $S = \sqrt{2S_{ij}S_{ij}}$  is the invariant measure of the mean flow strain rate.  $F_2$  is a blending function defined by:

$$F_2 = \tanh \left[ \max \left( \frac{2\sqrt{k}}{\beta^* \omega z}, \frac{500v}{z^2 \omega} \right) \right]^2, \quad (21)$$

where  $\beta^*$  is taken as 0.09. The transport equations for  $k$  and  $\omega$  for turbulent flows at high Reynolds number are as follows:

$$\frac{\partial k}{\partial t} + \frac{\partial(\bar{u}_j k)}{\partial x_j} = \frac{\partial}{\partial x_j} \left[ (v + \sigma_k v_T) \frac{\partial k}{\partial x_j} \right] + \tilde{P}_k - \beta^* k \omega, \quad (22)$$

$$\frac{\partial \omega}{\partial t} + \frac{\partial(\bar{u}_j \omega)}{\partial x_j} = \alpha S^2 - \beta \omega^2 + \frac{\partial}{\partial x_j} \left[ (v + \sigma_k v_T) \frac{\partial \omega}{\partial x_j} \right] + 2(1 - F_1) \sigma_{\omega 2} \frac{1}{\omega} \frac{\partial k \partial \omega}{\partial x_j \partial x_j}, \quad (23)$$

where the  $\tilde{P}_k = \min(P_k, 10\beta^* k \omega)$  is a limited production rate.  $F_1$  is another blending function defined by

$$F_1 = \tanh \left\{ \left\{ \min \left[ \max \left( \frac{\sqrt{k}}{\beta^* \omega z}, \frac{500v}{z^2 \omega} \right), \frac{4\sigma_{\omega 2} k}{CD_{k\omega} z^2} \right] \right\}^4 \right\}, \quad (24)$$

with  $CD_{k\omega} = \max \left( 2\sigma_{\omega 2} \frac{1}{\omega} \frac{\partial k \partial \omega}{\partial x_j \partial x_j}, 10^{-10} \right)$ . The constants in Equations (22) and (23) are computed by a blending function from the corresponding constants of the  $k-\epsilon$  and the  $k-\omega$  model via  $C = C_1 F + C_2 (1 - F)$ . These constants are :  $\sigma_{k1}=0.85$ ,  $\sigma_{k2}=1$ ,  $\alpha_1=5/9$ ,  $\alpha_2=0.44$ ,  $\beta_1=3/40$ ,  $\beta_2=0.0828$ ,  $\sigma_{\omega 1}=0.5$ ,  $\sigma_{\omega 2}=0.856$ .

In this work, the standard deviation of the horizontal wind speed needs to be computed from the simulation in order to make comparison to the conditional averaged wind speed standard deviation obtained on each met-tower. This quantity can be calculated as the square root of the sum of variances of the horizontal wind components<sup>40,54</sup> as

$$\sigma_Q = \sqrt{\sigma_{u_x}^2 + \sigma_{u_y}^2}, \quad (25)$$

where  $\sigma_{u_x}^2 = \overline{u'_x u'_x}$  and  $\sigma_{u_y}^2 = \overline{u'_y u'_y}$  are obtained from the first two diagonal elements of the density-normalized Reynolds stress tensor  $T_{ij}/\rho = \frac{2}{3}k\delta_{ij} - 2v_T S_{ij}$ .

### 3.3 | Domain selection and mesh generation

Based on the most frequent wind direction (227°) obtained at 57-m AGL on the reference tower SM 03 during the summer, the orientation of the computational domain is set-up by aligning the x-axis with this direction. Thus the y-axis indicates the crosswind-direction and z-axis indicates the altitudinal direction. A domain size of 18 km × 15 km × 1.2 km in the x-, y- and z-directions, respectively, is selected (shown in Figure 6) and denoted as “D1” so that all of the met-towers within SM site are included and located at least 1 km away from the boundaries. Note that the Coriolis force term in Equation (13) needs to be re-projected from the conventional geographic coordinate system (where x-direction is from west to east and y-direction is from south to north) onto the current coordinate system. The surface mesh is generated with a horizontal grid resolution of 15 m, which is chosen as two times finer than the resolution of the original SRTM data so that the topographic features can be resolved more smoothly. The vertical mesh is created with a tanh-based function<sup>55</sup> such that the vertical grid spacing is stretched from 4 m at the surface adjacent cells to 43 m at the cells adjacent to the top boundary. The total number of the grid cells is 1200 (nx) × 1000 (ny) × 100 (nz) = 120 million and the mesh has an average and maximum non-orthogonality of 5 and 49, respectively. A close-up view of the computational mesh is shown in Figure 7. Note that met-tower SM 04 is not considered in the present work since it is located very close to the inlet plane.

In addition, a small domain with the size of 6 km × 3.5 km × 1.2 km in x-, y-, and z-directions, respectively, is chosen to conduct the inflow generation and mesh independence study at a reduced computational cost. The small domain which is located in the top left corner of the bigger domain is also shown in Figure 6 and denoted as “D2”. The inlet, top and one of the lateral boundaries of D2 are just a portion of their corresponding boundaries on D1. The reference tower SM 03 is located within both domains.

The flat precursor simulations are performed on a domain size of 3 km × 0.075 km × 1.3 km with 200 (nx) × 5 (ny) × 110 (nz) cells in the x-, y- and z-directions, respectively. A similar grid stretching in the z-direction as in the terrain case is applied with a slightly higher resolution to ensure proper interpolation for the flow mapping from the precursor to the inlet of the complex terrain mesh.

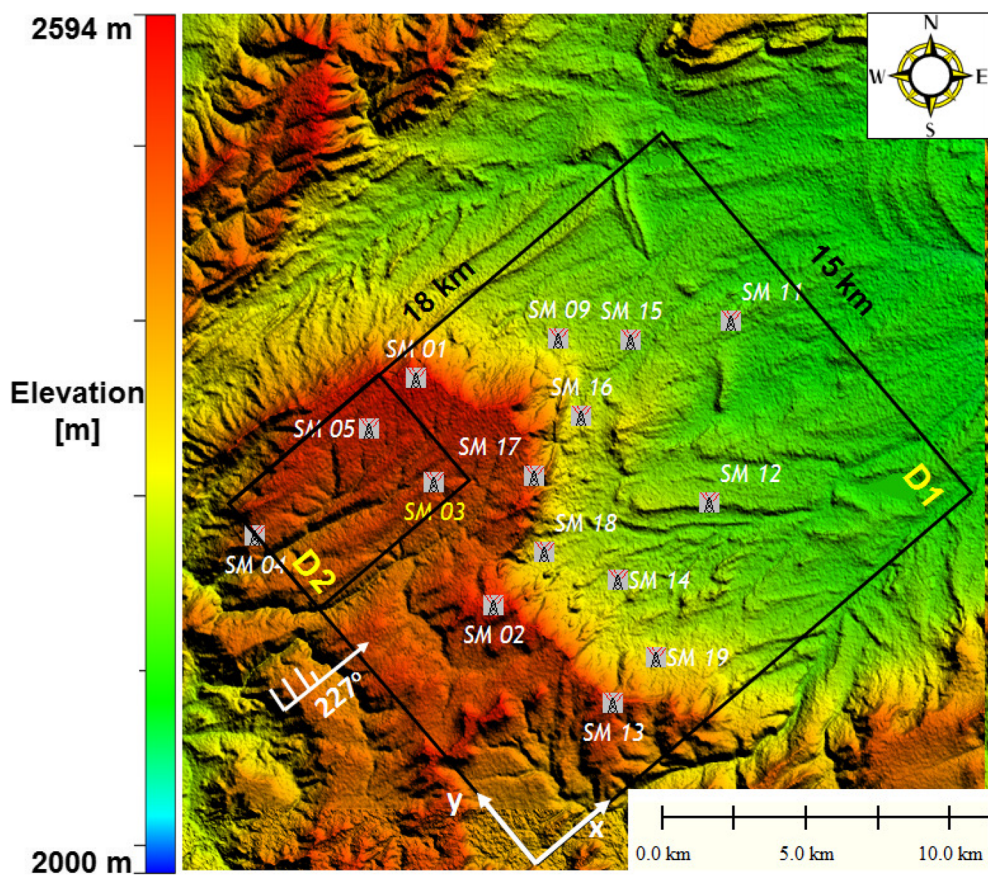


**FIGURE 6** Selection of simulation domains [Colour figure can be viewed at [wileyonlinelibrary.com](http://wileyonlinelibrary.com)]

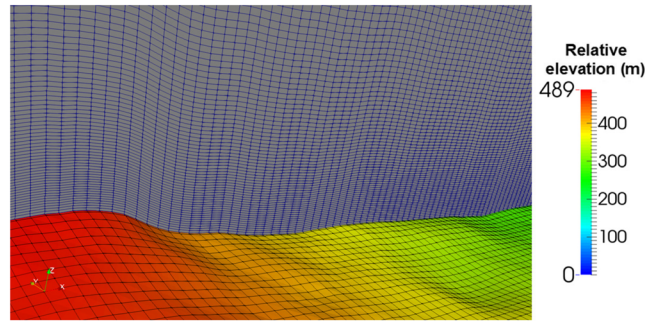


**FIGURE 7** Close-up view of the mesh [Colour figure can be viewed at [wileyonlinelibrary.com](http://wileyonlinelibrary.com)]

### 3.4 | Boundary conditions

#### 3.4.1 | Inflow and outflow boundary conditions

The appropriate inflow conditions for the RANS-ABL simulation need to be generated so that the conditional averaged wind speed and standard deviation measured at the reference tower SM 03 can be reproduced. Several steps of an iterative procedure are required. The iteration starts with setting  $z_0=0.01$  m, and the conditional sampling procedure of the met-tower data is conducted. Then, a precursor simulation performed with the same  $z_0$  is driven by an adjustable pressure gradient  $\partial p_0 / \partial x_i$  such that the simulated wind speed at 57-m AGL ( $Q_{prec}^{57m}$ ) equals the conditional averaged wind speed  $Q_{cond}^{57m}$  at the reference tower. The flow variables ( $\bar{u}_i$ ,  $k$ , and  $\epsilon$  or  $\omega$ ) are sampled in the vertical direction (since the flow is statistically one-dimensional) once the simulation has reached a steady state. The profiles of  $\bar{u}_i(z)$ ,  $k(z)$  and  $\epsilon(z)$  or  $\omega(z)$  are subsequently mapped onto the terrain-following mesh at the inlet boundary of the smaller D2 domain based on the relative height above the ground.<sup>56</sup> The outlet boundary condition for the terrain simulations is specified as  $\tilde{p}_{mod} = 0$  and Neumann zero-gradient conditions for all other flow variables.

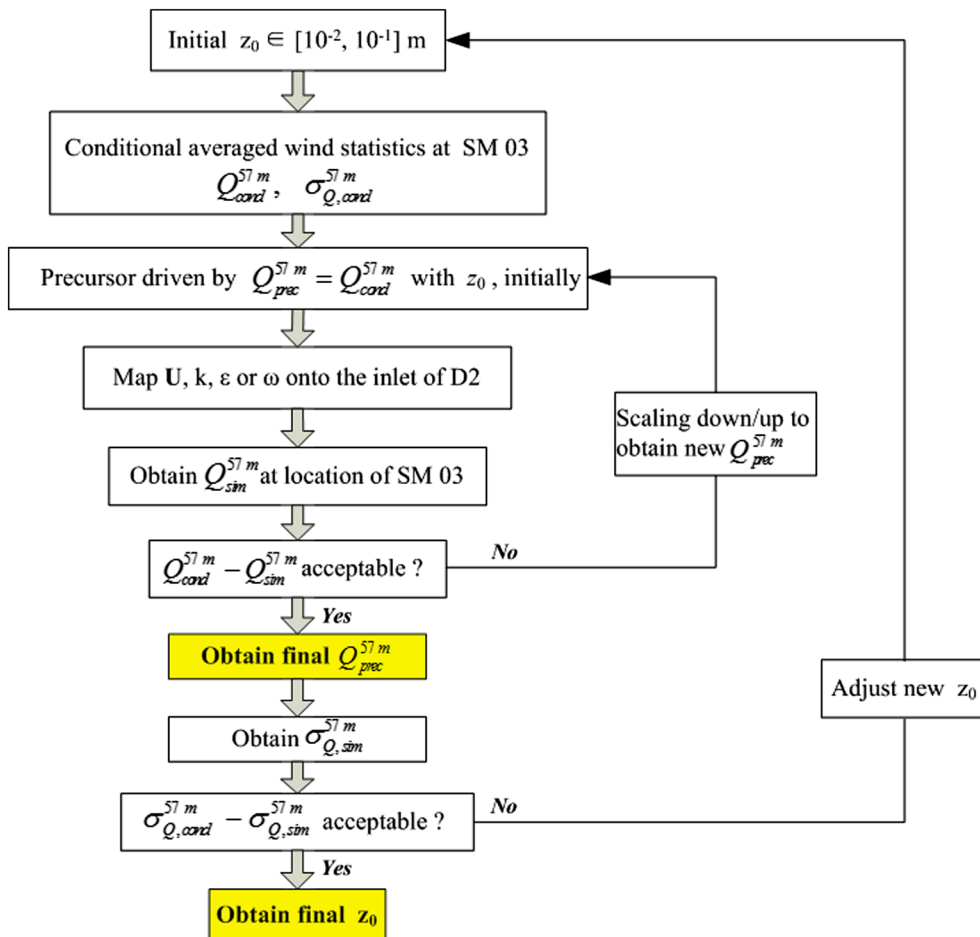


**FIGURE 8** The iterative approach to obtain the reasonable  $z_0$  and appropriate inflow conditions for the ABL terrain simulation [Colour figure can be viewed at [wileyonlinelibrary.com](http://wileyonlinelibrary.com)]

Due to a slight up-slope of the terrain between the inlet boundary and tower SM 03, the simulated wind speed at 57-m AGL  $Q_{\text{sim}}^{57m}$  on the location of SM 03 is slightly over-predicted compared with the conditional averaged tower data  $Q_{\text{cond}}^{57m}$  when the terrain simulation uses an inlet velocity profile from a precursor with  $Q_{\text{prec}}^{57m} = Q_{\text{cond}}^{57m}$ .<sup>56,57</sup> To account for the acceleration over the up-slope terrain,  $Q_{\text{prec}}^{57m}$  needs to be slightly decreased. This adjustment is done iteratively as shown in Figure 8 until the difference between  $Q_{\text{sim}}^{57m}$  and  $Q_{\text{cond}}^{57m}$  is acceptable. In addition, the predicted standard deviation  $\sigma_{Q,\text{sim}}^{57m}$  should also match the measured value  $\sigma_{Q,\text{cond}}^{57m}$  based on the chosen  $z_0$ . In the first iteration, the standard deviation was under-predicted, and thus, the initial guess of  $z_0 = 0.01 \text{ m}$  has to be increased. Note that changing  $z_0$  requires to recalculate the conditional met-tower statistics. Fortunately, the conditional mean wind speed profiles obtained from the met-tower data and the simulation are not sensitive to small adjustments of  $z_0$ ; thus, the driving wind speed of the precursor  $Q_{\text{prec}}^{57m}$  does not have to be re-adjusted. The iterative procedure is stopped with the final roughness value of  $z_0=0.035 \text{ m}$ , leading to a close agreement of  $Q_{\text{sim}}^{57m}$  and  $\sigma_{Q,\text{sim}}^{57m}$  with the corresponding conditional averaged wind statistics at the reference tower SM 03. Table 1 summarized the results for both turbulence models using  $z_0=0.035 \text{ m}$ .

**TABLE 1** Comparison of the wind statistics at 57-m AGL in the flat precursor simulation, the terrain simulation over D2, and the conditional tower data using  $z_0=0.035 \text{ m}$

Wind at 57-m AGL	Precursor Simulation	Ref. Tower SM 03		
		Terrain Simulation	Tower Data	error
Mean wind speed (m/s) [ $k-\epsilon$ ]	8.32 ( $Q_{\text{prec}}^{57m}$ )	8.66 ( $Q_{\text{sim}}^{57m}$ )	8.57 ( $Q_{\text{cond}}^{57m}$ )	≈ 1%
Wind speed standard deviation (m/s) [ $k-\epsilon$ ]	0.94	0.92 ( $\sigma_{Q,\text{sim}}^{57m}$ )	0.91 ( $\sigma_{Q,\text{cond}}^{57m}$ )	≈ 1%
Mean wind speed (m/s) [SST $k-\omega$ ]	8.32	8.74	8.57	≈ 2%
Wind speed standard deviation (m/s) [SST $k-\omega$ ]	0.92	0.88	0.91	≈ 3%

### 3.4.2 | Lateral and top boundary conditions

On the lateral boundary, the irregular terrain shape may change the flow direction locally and the effect of the Coriolis force will induce the veering of the mean wind with height. Therefore, the lateral boundaries should be capable of allowing for spatially varying inflow and outflow. The coupled velocity-pressure boundary conditions are implemented based on the direction of the local mass flux computed at the center of each cell adjacent to the boundaries<sup>56</sup> using the most up-to-date velocity. The mathematical expression for the velocity and modified pressure boundary conditions are

$$\text{If } \phi_c < 0 \text{ (inward mass flux), then } u_{b,t} = u_{c,t}, \quad u_{b,n} = \frac{\phi_c}{A_b}, \quad \bar{p}_{mod,b} = \bar{p}_{mod,c} \text{ If } \phi_c \geq 0 \text{ (outward mass flux), then } u_{b,t} \\ = u_{c,t}, \quad u_{b,n} = u_{c,n}, \quad \bar{p}_{mod,b} = 0$$

where  $\phi_c$  is the mass flux computed at the center of each boundary cell.  $u_{c,t}$  and  $u_{c,n}$  are the velocity components tangential and normal to the boundary face, respectively, which are taken at the center of the boundary cell.  $u_{b,t}$  and  $u_{b,n}$  are the velocity components tangential and normal to the boundary face, respectively, which are stored at the center of the boundary face.  $A_b$  is the area of the boundary face.  $\bar{p}_{mod,b}$  and  $\bar{p}_{mod,c}$  are the modified pressures at the face center and the center of the boundary cell, respectively.

According to the conditional met-tower analysis (see Section 2.4.3), the wind speeds at the met-towers located downstream of the main ridge (steep down-slope) do not slow down significantly even though there is a large expansion of the cross-stream area. If a typical simple slip-wall boundary condition would be applied at the top of the domain, one would have to use a domain with a height of 13 km to keep the flow declaration behind the main ridge at a level less than 3% (comparable to the accuracy of the inlet profile generation).<sup>57</sup> To keep the computational cost low, we decide to adopt a top boundary condition that does allow for both inflow and outflow and the top boundary can thus be placed at a much lower height. To achieve these requirements, we adopt the same condition for velocity as on the lateral boundaries but fix the modified pressure uniformly to  $\bar{p}_{mod,b} = 0$  on the top boundary.<sup>57</sup> Neumann zero-gradient conditions are specified for other flow variables on both top and lateral boundaries. The developed lateral and top boundary conditions are only used in the terrain simulations and the flow is driven by the prescribed inflow conditions obtained from the precursor simulation, i.e., no driving pressure gradient  $\partial p_0 / \partial x_i$  is applied.

### 3.4.3 | Surface boundary condition

The standard empirical rough wall function<sup>58</sup> is implemented on the surface boundary using a wall normal coordinate denoted by  $n$  to highlight how the terrain influences the surface conditions through the misalignment of the  $z$ -direction and the local surface normal vector  $\vec{n}$ . Based on the assumption that the TKE is constant within the logarithmic law region, a zero gradient boundary condition is specified for  $k$ . A zero gradient boundary condition is also applied for the modified pressure. Instead of explicitly adding the wall shear stress as a source term in the mean momentum equations, we follow the common approach and prescribe a no-slip boundary condition for the velocity at the wall surface. The correct shear stress is then obtained by adjusting the eddy viscosity value at the wall such that the effective stress is equal to the value required by the logarithmic law. This enables to keep the implicit treatment of the Laplacian term in Equation (15) with an eddy viscosity at the wall given by<sup>49,59</sup>

$$v_{T,w} = v \cdot \left[ \frac{\frac{\kappa d_p^+}{d_p + z_0} - 1}{\ln \frac{d_p + z_0}{z_0}} \right], \quad d_p^+ = \frac{d_p u_*}{v}, \quad d_p = \vec{x}_P - \vec{x}_w \cdot \vec{n}, \quad (26)$$

where the subscript  $w$  denotes a value at the surface, the subscript  $P$  indicates the value of the quantity at the wall adjacent cell center. The friction velocity is calculated as by  $u_* = C_\mu^{1/4} k_p^{1/2}$ .<sup>11</sup>

The production term of turbulent kinetic energy at the wall adjacent cell center is implemented in OpenFOAM according to the law of the wall (LOTW) to be

$$P_{k,p} = (v_{T,w} + v) \frac{\frac{\partial \bar{u}}{\partial n}|_p C_\mu^{1/4} \sqrt{k_p}}{\kappa d_p}. \quad (27)$$

In the  $k-\epsilon$  model, the condition for the dissipation rate  $\epsilon$  can be obtained by using a balance between production and dissipation. The corresponding value at the wall adjacent cell center set by the wall function<sup>58</sup> as

$$\epsilon_p = \frac{u_*^3}{\kappa d_p}. \quad (28)$$

In the SST  $k-\omega$  model, the specific dissipation rate at the wall adjacent cell center is set to be

$$\omega_p = \frac{\sqrt{k_p}}{C_\mu^{1/4} k d_p}. \quad (29)$$

### 3.5 | Numerical implementation

The RANS governing equations are solved with a collocated finite volume method for arbitrary unstructured grids implemented in the open source CFD software OpenFOAM through the wind farm simulation software package SOWFA. The flat precursor simulations and the terrain ABL simulations are conducted based on modified versions of the SOWFA “ABLSolver” and “ABLTerrainSolver,” respectively. The “Gauss linear corrected” scheme, which is similar to a second-order central differencing scheme, is used for the discretization of the Gradient and Laplacian terms. The divergence term uses the “Gauss upwind” scheme during the initialization of the flow field to ensure numerical stability. For the final results, the “Gauss linear upwind” scheme with second-order accuracy is applied. The computation of fluxes through finite-volume faces is implemented through a procedure akin to the Rhie and Chow<sup>60</sup> interpolation to avoid decoupling of the pressure and velocity fields at the cell level. The time discretization is chosen as “backward implicit” scheme which uses the field values from the current and two successive old time step fields to assemble a second-order accurate temporal derivative.

A novel approach to calculate the TKE production in Equation (19) is adopted by following a suggestion of Richards and Hoxey<sup>58</sup> to reduce the commonly observed overshoot of the (TKE) very close to the surface. They found that the overshoot was caused when calculating the TKE production based on the cell centered velocity gradient and eddy viscosity, whereas the shear stress in the momentum equation was calculated using a face centered gradient through the numerical implementation of the Laplacian. The value of the TKE production from the cell centered calculation actually exceeds the dissipation in the cells near the surface thus causing the overshoot. Note that the first cell values are correct as both production and dissipation values are set to the equilibrium boundary layer values through the wall functions. A solution to this issue for flat ABL simulations using a finite difference solver was proposed by Richards and Hoxey<sup>58</sup> based on averaging the square of the shear stress (using face centered velocity gradients) values on the north and south faces. Here, we generalize this idea to work for unstructured finite volume methods using a face area weighted average

$$P_{k,p} = \frac{1}{v_{T,p}} \frac{\sum_{f \in \text{cell faces}} 2v_{T,f}^2 \tilde{S}_{ij,f} \tilde{S}_{ij,f} A_f}{\sum_{f \in \text{cell faces}} A_f}, \quad (30)$$

where subscript  $f$  indicates a value at the face center, subscript  $P$  denotes a value at the cell center, and  $A_f$  denotes the face area. The strain rate tensor at the face center  $\tilde{S}_{ij,f}$  is calculated using a velocity gradient at the face center  $\nabla \vec{u}_f$  with a face normal component equal to the surface normal gradient calculated using the “tight” face-centered stencil<sup>61</sup>

$$\nabla \vec{u}_f = \langle \nabla \vec{u} \rangle_f + \left[ \frac{\vec{u}_F - \vec{u}_P}{\|\vec{d}_{PF}\|} - (\langle \nabla \vec{u} \rangle_f \cdot \vec{e}_{PF}) \right] \vec{e}_{PF}, \quad (31)$$

where we use vector notation to simplify the presentation. Here,  $F$  stands for the neighbor cell center of  $P$  on face  $f$ ,  $\vec{d}_{PF} = \vec{x}_F - \vec{x}_P$  is the vector joining the cell centers and  $\vec{e}_{PF} = \vec{d}_{PF}/\|\vec{d}_{PF}\|$  is the corresponding unit vector, and  $\langle \nabla \vec{u} \rangle_f$  denotes the cell centered gradient linearly interpolated to the face. Using this gradient approximation is critical as it mimics the simple face centered finite difference formula.<sup>58,62</sup> The validity and quality of this approximation is shown in Section 4.1.

Since the RANS simulation of the ABL flow will eventually reach a steady state, the PIMPLE algorithm<sup>63</sup> which is a combination of both PISO (Pressure Implicit with Splitting of Operation)<sup>64</sup> and SIMPLE (Semi-Implicit Method for Pressure Linked Equations)<sup>65</sup> algorithms is adopted to solve the pressure-velocity coupling to speed up the computation and convergence rates. During each time step six pressure-momentum corrections (outer loop) are performed. Within one outer loop, pressure correction is conducted twice and one non-orthogonal correction is adopted on the last corrector<sup>61</sup> (for terrain simulations only). By using the PIMPLE algorithm, the maximum Courant-Friedrich-Levy (CFL) number in the simulations could be set as high as 15.0 which speeds up the simulation process without losing stability and accuracy.

The algebraic equations resulting from the discretization of the momentum,  $k$ ,  $\epsilon$  or  $\omega$  transport equations are solved with a diagonal-based incomplete-lower-upper (DILU) preconditioner followed by a preconditioned bi-conjugate gradient (PBiCG) linear system solver. Solving for the modified pressure  $\tilde{p}_{mod}$ , which is the most time-consuming step of the algorithm, is done with the preconditioned conjugate gradient (PCG) solver together with a geometric agglomerated algebraic multigrid (GAMG) preconditioner. The solver is parallelized with message passing interface (MPI) technique. The computational mesh and fields are decomposed for parallel processing using Scotch<sup>66</sup> which requires no geometric input from the user and attempts to minimize the number of processor boundaries. The simulation requires about 8 hours computational time to reach the steady

state with the final residuals of each variable below  $10^{-7}$ . The time step is adjustable and it varies roughly between 4.8 sec and 7.6 sec during the entire simulation. A simulation of the large domain D1 takes about 5 hours of execution time on 2412 processors.

## 4 | SIMULATION RESULTS

### 4.1 | Precursor simulations of ABL over flat surface

The flat precursor simulations are performed with periodic boundary conditions on the lateral boundaries, a slip-wall on the top boundary, and the surface boundary condition with  $z_0 = 0.035$  m. The simulations are driven with a pressure gradient to enforce the required wind speed at AGL = 57 m of  $\bar{u}_x = 8.32$  m/s,  $\bar{u}_y = \bar{u}_z = 0$ . With the Coriolis force term activated, a horizontally homogeneous ABL develops with a typical Ekman wind profile and an ABL height of 1.1 km as shown in Figure 9. As expected, in the atmospheric surface layer (ASL, typically the bottom 10% of the ABL height<sup>35</sup> or  $z/z_0 < 4 \times 10^3$ ) the horizontal mean wind speed  $Q$  follows the LOTW

$$Q = \frac{u_*}{k} \ln \frac{z + z_0}{z_0}, \quad (32)$$

but deviates from it at greater elevations.

To further assess how well the ASL is simulated, the normalized horizontal mean wind speeds obtained from the  $k-\epsilon$  and the SST  $k-\omega$  models are compared to the LOTW scaling as shown in Figure 10. Both turbulence models predict mean wind speeds that follow the LOTW scaling very closely. For comparison, the results from the  $k-\epsilon$  model using the original cell centered calculation of  $P_k$  is also shown in Figure 10 (the SST  $k-\omega$  model results are similar and are not shown). The results follow the LOTW scaling for most of the surface layer except for the first two cell levels above the surface where an under-prediction can be observed.

The nondimensional turbulent kinetic energy profiles (normalized by  $u^*$ ) obtained from the two RANS models are compared to the constant LOTW value implied by the turbulence model<sup>58,62</sup> and to the  $k-\epsilon$  model with cell centered  $P_k$  calculation in Figure 11. The new  $P_k$  calculation does reduce the overshoot for both turbulence models and the two model results are almost identical. The predicted TKE profile is not constant but decays slowly with height due to the Coriolis force and the adopted top boundary condition. Although the new formulation for the production Equation (30) does not completely remove the overshoot, it is more general than the procedure of Richards et al.,<sup>58,62</sup> and it is used in all the terrain simulations. However, in the terrain results which focus on the data acquisition range (20 to 70-m AGLs) of the met towers, no appreciable difference between cell centered and new production calculation is observed.

### 4.2 | Mesh independence study

For the adopted steady-state RANS approaches, it is important to ensure that the converged solution is independent of the mesh resolution. The mesh independence study focuses on the horizontal grid resolution which is significantly coarser than that in the vertical direction. The study is performed by using three different grids over the complex terrain of the D2 domain, each with twice the number of grid points in the horizontal directions as the previous grid. The number of grid points and the stretching function in the vertical direction remains the same for all the grids. Figure 12 shows the profiles of the mean wind speed computed at the location of the reference tower SM 03 from the solutions with coarse (30

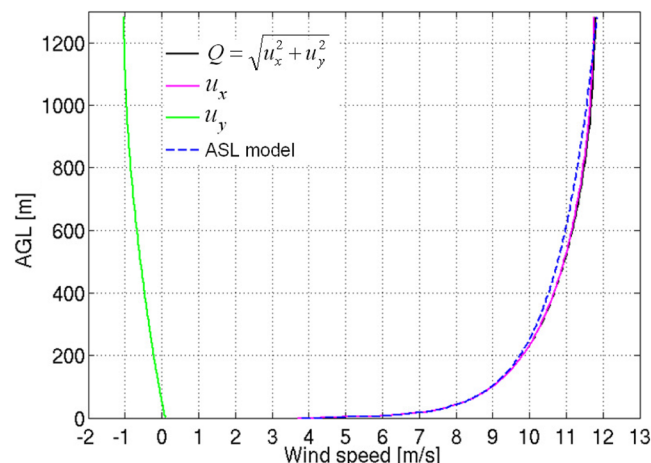


**FIGURE 9** Structure of the precursor ABL over flat surface obtained with the  $k-\epsilon$  model [Colour figure can be viewed at [wileyonlinelibrary.com](http://wileyonlinelibrary.com)]

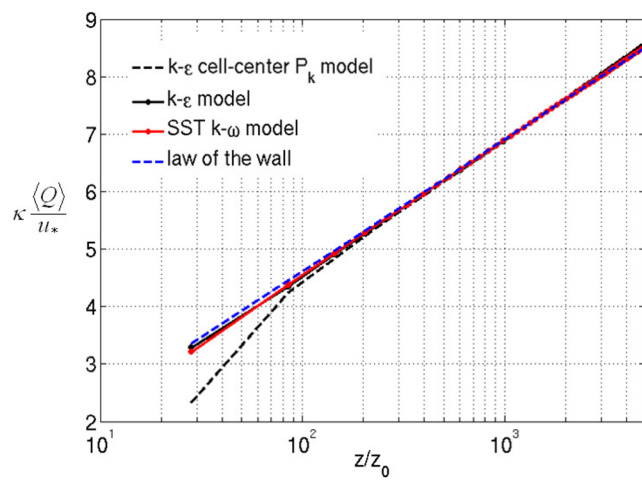


**FIGURE 10** Comparison of the normalized horizontal mean wind speeds to LOTW from precursor simulations [Colour figure can be viewed at [wileyonlinelibrary.com](http://wileyonlinelibrary.com)]

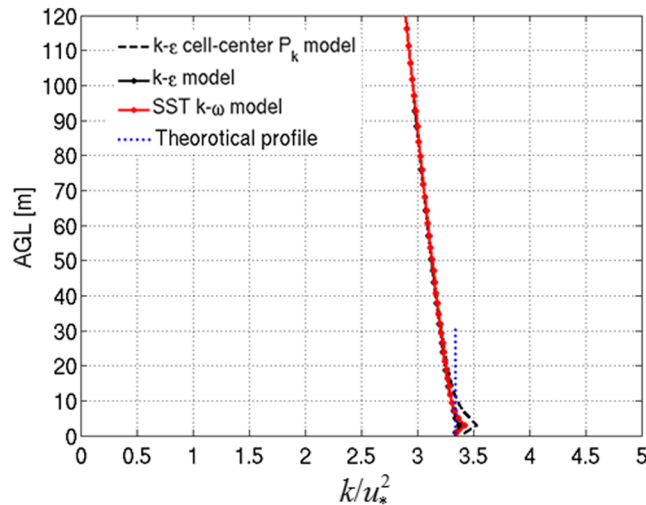


**FIGURE 11** Comparison of the normalized  $k$  profiles to the theoretical RANS profile from precursor simulations [Colour figure can be viewed at [wileyonlinelibrary.com](http://wileyonlinelibrary.com)]

m), medium (15 m), and fine (7.5 m) mesh resolution, respectively. It is shown that the difference between the fine and medium meshes is approximately two times smaller than that between medium and coarse meshes within the atmospheric surface layer.

The simulated mean wind speed at 57-m AGL  $Q_{\text{sim}}^{57\text{m}}$  at SM 03 is used as an indicator for the grid convergence using the Richardson extrapolation method.<sup>67</sup> Richardson extrapolation is a method for obtaining a higher-order estimate of the continuum value (at zero grid spacing) from a series of lower-order discrete values. The order of convergence observed from these computed mean speed values on the three grid levels has been computed as 1.6, which is comparable to the theoretical order of convergence of 2.0. By using the mean wind speed values at the two finest grids, which are 8.58 m/s for 15 m resolution and 8.59 m/s for 7.5 m resolution, respectively, the mean wind speed at zero grid spacing is estimated as  $8.60 \text{ m/s} \pm 0.1 \text{ m/s}$ . It is obvious to see that as the grid spacing is refined, the mean wind speeds approach an asymptotic zero-grid spacing value. The value of 8.59 m/s computed from the fine mesh falls within the estimated range at zero grid spacing, but it would be computationally too costly to use this fine resolution in simulations of the large D1 domain. The mean wind speed obtained from the simulation with the medium mesh resolution falls within an acceptable error range of 0.2% of the zero grid spacing wind speed. Therefore, the chosen horizontal grid spacing ( $\Delta x = \Delta y = 15 \text{ m}$ ) is reasonable in terms of accuracy and computational cost.

#### 4.3 | Influence of the domain height

Even with the realistic boundary conditions adopted at the top of the computational domain, it is worthwhile verifying that the chosen height of the computational domain does not affect the simulation results at the tower locations. A higher computational domain with a height of 3 km is

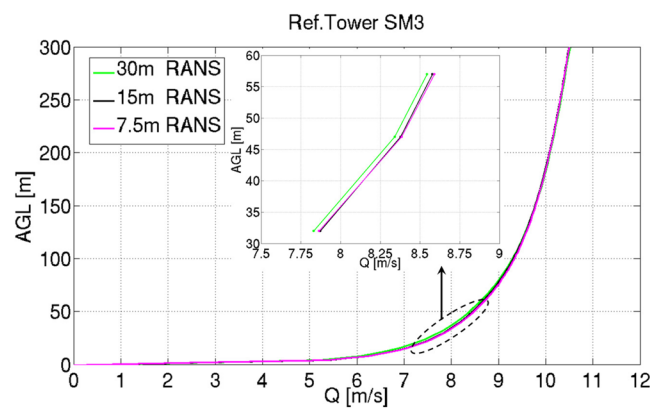


**FIGURE 12** Simulated mean wind profiles on the location of SM 03 using small computational domain with 7.5-, 15-, and 30-m horizontal mesh resolutions [Colour figure can be viewed at [wileyonlinelibrary.com](#)]

created over the terrain surface of D1. The grid spacing below the height of 1.2 km is kept exactly the same as on D1 while the vertical grid resolution above 1.2 km is uniformly set to  $\Delta z = 43$  m. The driving force of the flow within the higher domain, i.e., the inflow conditions of  $\bar{u}_i(z)$ ,  $k(z)$  and  $\epsilon(z)$  or  $\omega(z)$ , are obtained from a corresponding precursor simulation with the same driving conditions as those obtained for D1.

The mean wind profiles for some representative met-towers including SM 03 (located upstream of the main ridge), SM 16 (behind the ridge), and SM 11 (far away downstream of the ridge) from 20 to 70-m AGL are compared in Figure 13. The mean wind profiles obtained from the simulations with different domain heights are in good agreement with each other (less than 3 % difference) at the selected tower locations. The comparisons at other tower locations show even smaller differences, which is not shown for the sake of brevity. Thus, it can be concluded that the influence of the domain height on the simulation result is greatly reduced by using the top boundary condition presented in Section 3.4.2, and the accuracy of simulation results is not affected by the chosen 1.2-km domain height.

#### 4.4 | Qualitative analysis of simulation results

To get a better understanding of how the terrain modifies the flow field within the ASL, the horizontal mean wind speed  $Q$  taken at 57-m AGL over the entire domain from the SST  $k-\omega$  models (corresponding to the highest AGL used for the conditional sampling of the tower data) is shown in Figure 14 A. Recall that the precursor simulation is driven by a constant horizontal mean wind speed  $Q_{prec}^{57m} = 8.32$  m/s. Thus, the value of  $Q$  along the y-axis at the inlet of the domain in the figure is uniformly  $Q^{57m}(0, y) = Q_{prec}^{57m}$ . The most striking feature in the mean wind speed contour plots is that it closely resembles the contour plot of the terrain relative elevation as shown in Figure 14B. The Miller hill rim (highest elevation region) is clearly visible as a high-speed region with  $Q$  around 10 m/s, followed by the low-speed region ( $Q$  around 6 m/s) located just downstream of the rim. It takes about 2 km downstream of the Miller hill rim for the flow to recover to the inflow wind speed. The extremely low wind speed near SM 13 clearly hints that a recirculation region is formed after the boundary layer has separated on the lee side of the steep ridge. The impact of several other smaller scale terrain features on the wind speed are also visible: low wind speeds corresponding to “valleys” (e.g., the valley located upstream of SM 02 at  $x \approx 2$  km,  $6 \text{ km} \leq y \leq 9 \text{ km}$ ) and higher wind speeds corresponding to escarpments (e.g., the “double hill” located within the region between  $14 \text{ km} \leq x \leq 16 \text{ km}$  and  $12 \text{ km} \leq y \leq 14 \text{ km}$ ). The horizontal mean wind speeds obtained from the  $k-\epsilon$  model (not shown) show similar

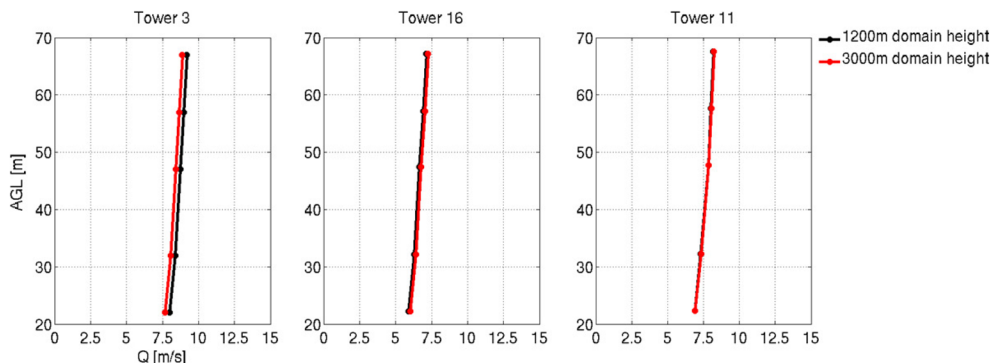


**FIGURE 13** Comparisons of simulated mean wind speed profiles at representative locations with different domain heights [Colour figure can be viewed at [wileyonlinelibrary.com](#)]

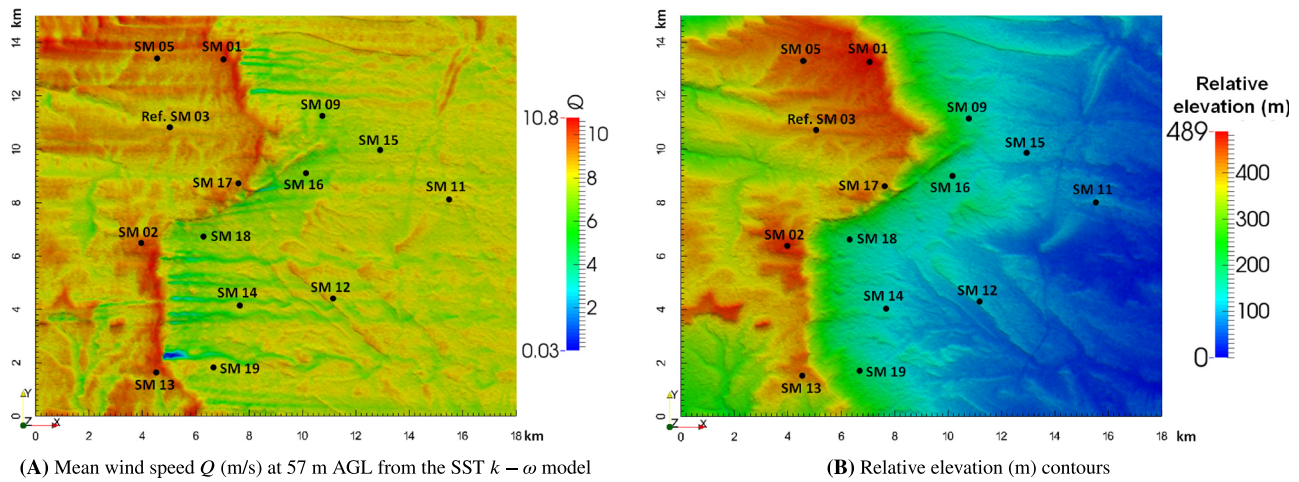


**FIGURE 14** Mean flow field and the relative elevation over the entire domain [Colour figure can be viewed at [wileyonlinelibrary.com](http://wileyonlinelibrary.com)]

trends to those from the SST  $k - \omega$  except that fewer and less pronounced terrain-induced wake regions behind the main ridge of the Miller hill are predicted by the  $k - \epsilon$  model.

To visualize flow recirculation regions close to the surface, mean stream-wise velocity contour plots at 20-m AGL from both the  $k - \epsilon$  and SST  $k - \omega$  models are shown in Figure 15. A large recirculation region (negative velocity) near SM 13 is predicted by both turbulence models. Overall, significantly more and larger recirculation regions are predicted by the SST  $k - \omega$  model on the lee side of the Miller hill where the elevation gradients are large (see the marked areas in the figures). This observation confirms that the SST  $k - \omega$  model is more capable of predicting pressure induced flow separation and recirculation than the  $k - \epsilon$  model.<sup>15</sup>

The turbulence intensity contours at 57-m AGL from both  $k - \epsilon$  and SST  $k - \omega$  models are shown in Figure 16. The upper limit of the turbulence intensity color maps have been cropped down to  $TI < 0.22$  to increase the contrast in the plots. Similar to the discussions in Section 2.4.3, one can see a decrease of the turbulence intensity due to the favorable pressure gradients on the windward side of the hill and an increase due to the adverse pressure gradients on the leeward side of the hill. It should be noted that the increase of turbulence intensity on the leeward side of the hill is not only caused by the decreased wind speed but also by an actual increase in the wind speed standard deviation (not shown). Both turbulence models predict particularly large values (of  $TI > 0.2$ ) starting in the regions with boundary layer separation or that are close to separation. These regions of large turbulence intensity extend much farther downstream than the recirculation regions since the large TKE values produced in the shear layers of the recirculation regions are convected downstream (see discussion in next paragraph). Since the SST  $k - \omega$  model predicts more and larger recirculation regions it also predicts more regions with larger turbulence intensity values than the  $k - \epsilon$  model.

Contour plots of the relevant flow variables obtained from the  $k - \epsilon$  model in a stream-wise plane passing through the tower SM 05 are shown in Figure 17. The low stream-wise velocity region ( $\bar{u}_x < 7$  m/s) near the surface thickens to about 80-m AGL on the lee side of the hill and then

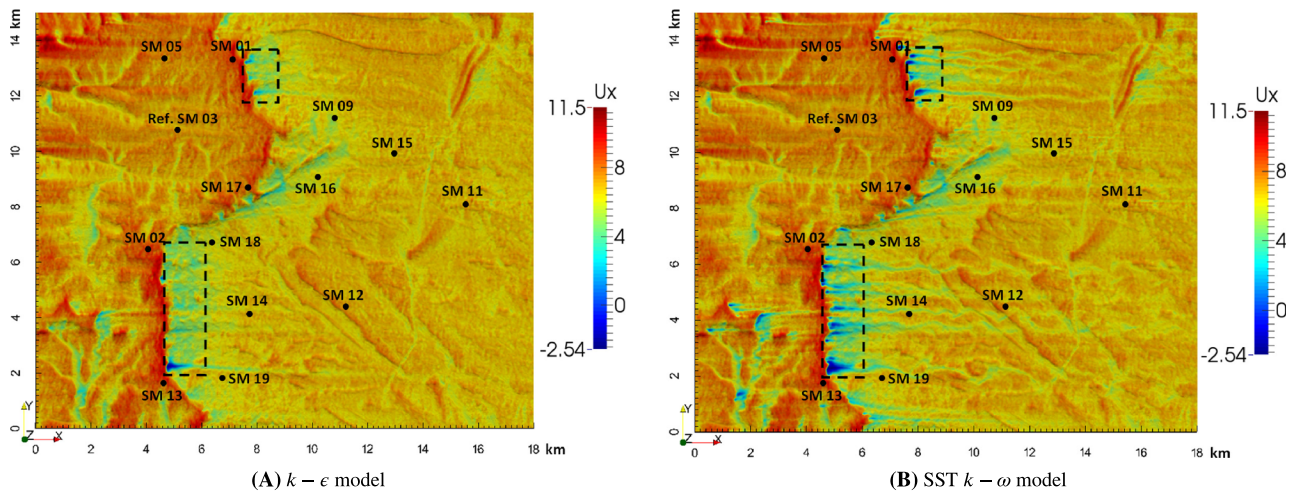


**FIGURE 15** Mean stream-wise velocity component  $\bar{u}_x$  (m/s) at 20-m AGL over the entire domain [Colour figure can be viewed at [wileyonlinelibrary.com](http://wileyonlinelibrary.com)]

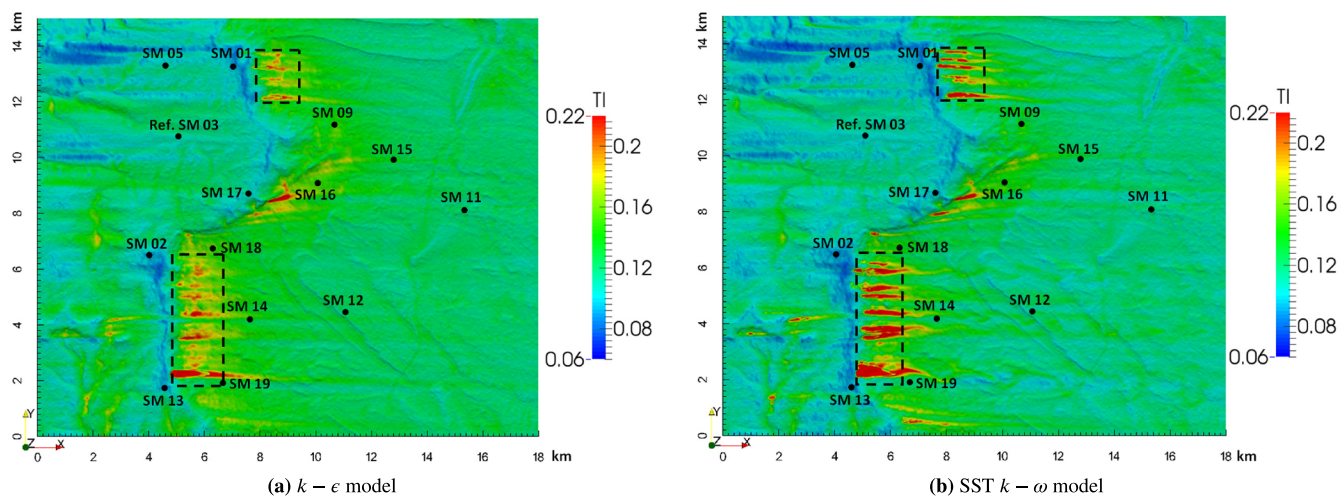


**FIGURE 16** Turbulence intensity contours at 57-m AGL over the entire domain [Colour figure can be viewed at [wileyonlinelibrary.com](http://wileyonlinelibrary.com)]

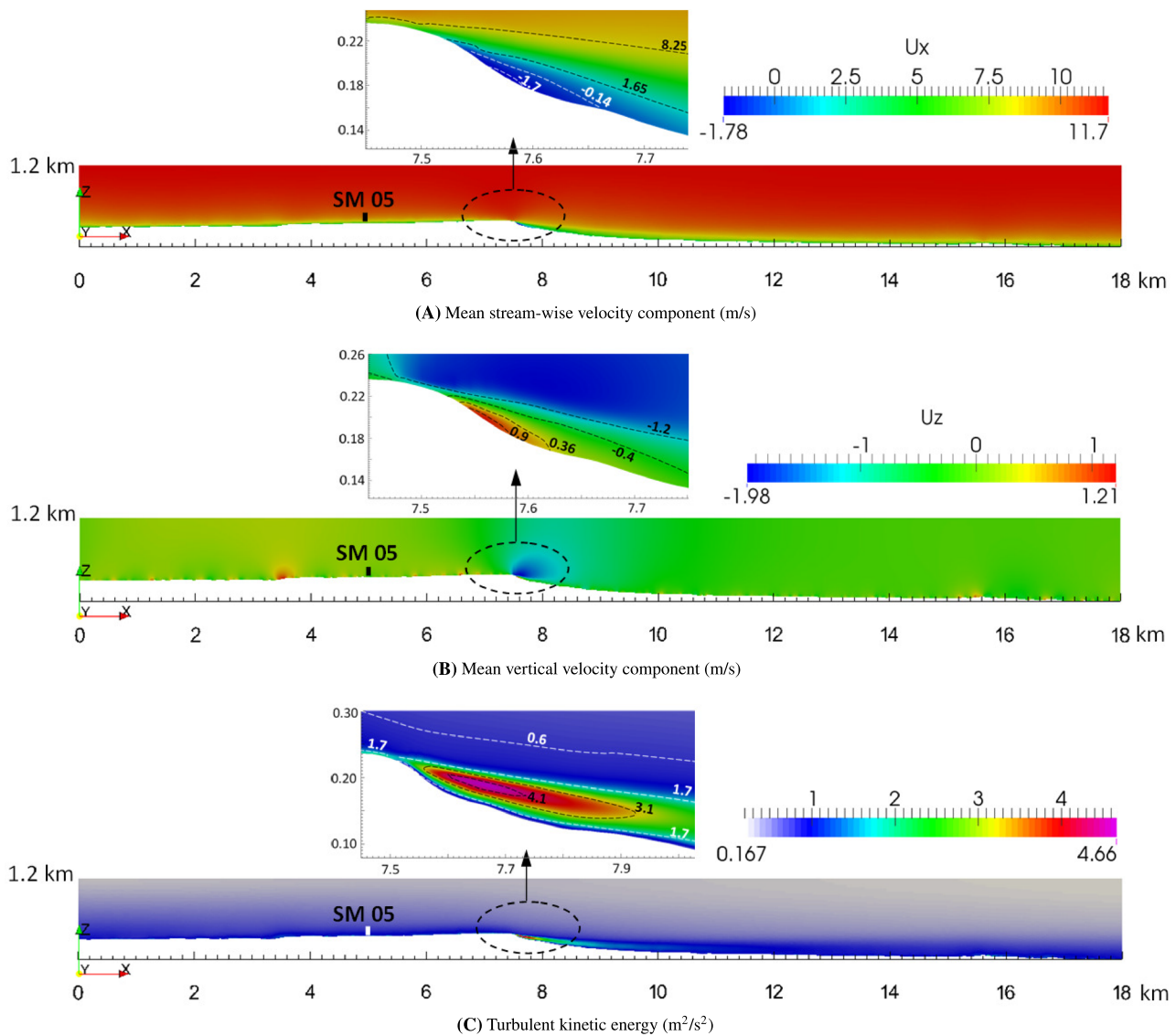


**FIGURE 17** Contour plots of flow variables in a stream-wise plane passing through SM 05 predicted by the  $k - \epsilon$  model [Colour figure can be viewed at [wileyonlinelibrary.com](http://wileyonlinelibrary.com)]

becomes noticeably thinner farther downstream as the flow accelerates, as seen in Figure 17A. Just downstream of the hill rim the flow separates over the steep segment, and a small recirculation region is formed with the flow moving upward ( $\bar{u}_z > 0$ ) as seen in Figure 17B. A strong shear layer with a larger production of turbulent kinetic energy is formed in the region between the recirculating near-surface flow and the downstream moving bulk flow as shown in Figure 17C. The turbulent kinetic energy values in the shear layer are about three times larger than the values observed upstream of the separation. The strong levels of turbulent kinetic energy are distributed by convection and turbulent diffusion, and slowly dissipated further downstream. The elevated  $k$  values can be observed as far as 2-km downstream of the Miller hill rim. The results obtained with the SST  $k-\omega$  model show a similar behavior but predict a stronger recirculation region associated with higher values of turbulent kinetic energy.

## 5 | COMPARISON BETWEEN SIMULATION RESULTS AND MET TOWER STATISTICS

The simulation results (from both  $k-\epsilon$  and SST  $k-\omega$  models) of the neutral ABL over the complex terrain within the SM wind site will be analyzed quantitatively by making comparisons with the conditionally averaged met-tower data for the wind direction, wind speed, and wind speed standard deviation.

### 5.1 | Upstream tower locations

For the met-towers (SM 01, 02, 03, 05, 13, and 17) located upstream of the main ridge, the predicted mean wind directions at 57-m AGL all fall within most frequent wind direction sector of the wind roses from the met-tower analysis as shown in Figure 18. Since the difference between the  $k-\epsilon$  and the SST  $k-\omega$  models are less than one degree at each tower, only the predicted mean wind directions from the  $k-\epsilon$  are shown as black lines. The range of the predicted mean wind direction is computed based on the mean stream-wise and cross-stream velocity components ( $\bar{u}_x$  and  $\bar{u}_y$ ) and the corresponding standard deviation components ( $\sigma_{u_x}$  and  $\sigma_{u_y}$ ) as

$$\Phi_{sim} = \Phi_{prev} - \arctan\left(\frac{\bar{u}_y \mp \sigma_{u_y}}{\bar{u}_x \pm \sigma_{u_x}}\right), \quad (33)$$

where  $\Phi_{prev}$  is the prevailing wind direction ( $227^\circ$  in the present case). The maximum and minimum values of  $\Phi_{sim}$  are regarded as the upper and lower limits of the predicted wind direction range, respectively.

Focusing on the tower observations portion in Table 2, all of the wind samples obtained at the reference tower SM 03 (the data set  $R_{S,V,N,t}^{57m}$ ) fall into the SW sector due to the adopted sampling condition of  $227^\circ \pm 5^\circ$ . For the data sets of the other met-towers, more than 60% of the wind samples fall into the SW direction, which makes it the most frequent wind sector for each of these towers. The one sector (either WSW or SSW) deviation from prevailing wind direction (SW) observed on some of the met-towers might be due to the local terrain effects. Overall, the predicted wind direction range from the two RANS models are almost identical with differences of less than  $1^\circ$ .

The comparison of the predicted mean wind speeds and the met-tower data for the towers located upstream of the main ridge is shown in Figure 19A. As a reference to gauge local variations, the wind speed of the reference tower SM 03 is added in the plots of each tower. Overall, the profiles computed by the  $k-\epsilon$  and the SST  $k-\omega$  models are almost identical (with no more than 1% difference between them). Starting from the reference tower SM 03, the predicted profiles match very well with the tower data, which means that the conditional averaged wind speed is well reproduced in both ABL simulations. In general, the simulation results show fairly good agreement with the measured data on most of the towers including the flow acceleration due to the favorable pressure gradient caused by the up-slope of the terrain. The largest difference is observed on tower SM 02 where the wind speed is over-predicted by 10% but the predictions still fall within the uncertainty range of the tower data analysis. Tower SM 02 is located on top of a “small hill” which rises about 60 m above the upstream terrain. Both turbulence models predict a speed-up compared to the reference tower SM 03, but it is somewhat surprising that the conditionally averaged tower data does not show such a speed-up. About 1 km upstream of SM 02, there is a small “canyon” that drops about 50 m below the upstream terrain. Both turbulence models predict a significant decrease in wind speed over the canyon but neither of them predicts boundary layer separation (see Figure 15). It is possible that separation actually occurs over the canyon and that the wind speed has not fully recovered as it accelerates over the hill at SM 02 thus leading to the observed lack of speed-up compared to SM 03. A confirmation of this explanation would require higher fidelity model simulations such as Reynolds Stress closure models or LES which will be the focus of a future study.

The comparison of the wind speed standard deviation between simulations and measurements is shown in Figure 19B. By design, the profiles predicted by both of the RANS models are in close agreement with the conditional averaged data at reference tower SM 03. The predicted values at the other towers fall within the range of uncertainty of the corresponding tower data. In general, the trend of the profiles predicted by the SST  $k-\omega$  model is quite consistent with that of the  $k-\epsilon$  model. However, the standard deviation values predicted by the SST  $k-\omega$  model are overall 5% to 8% smaller than the results predicted by the  $k-\epsilon$  model. This difference can be explained by the fact that the inflow values of the turbulent kinetic energy mapped from the precursor simulation using the SST  $k-\omega$  model are about 5% lower than those obtained by the  $k-\epsilon$  model near the surface.

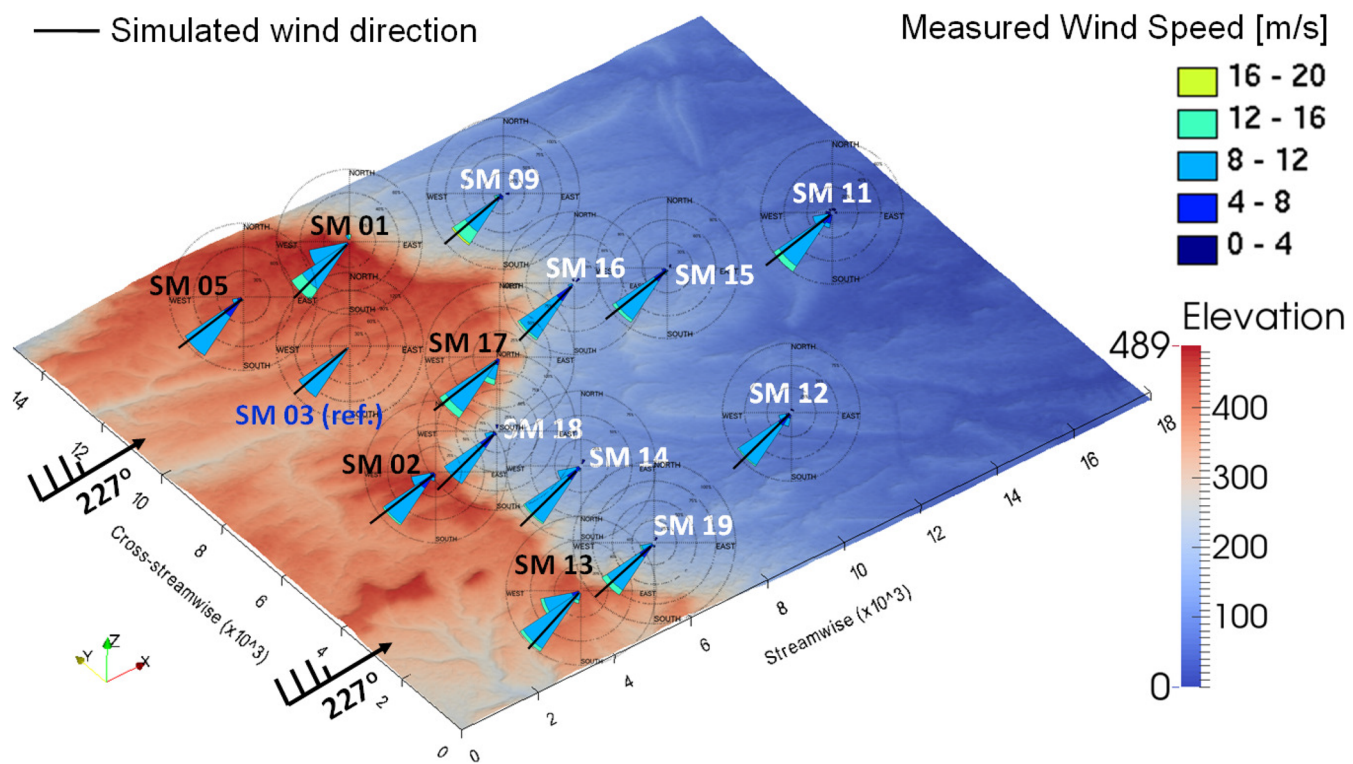


**FIGURE 18** Conditional averaged met-tower data in form of wind roses at 57-m AGL under neutral stability condition [Colour figure can be viewed at [wileyonlinelibrary.com](http://wileyonlinelibrary.com)]

**TABLE 2** Comparison of the predicted wind direction ranges and the observed most frequent wind direction sectors at 57-m AGL on each met-tower located ahead of the main ridge

Met-tower	Tower Observations		RANS Simulated Wind Direction $\Phi_{sim}$ [°]	
	Most Frequent Wind Sector [°]	Frequency	$k-\epsilon$	SST $k-\omega$
SM 01	213.75 - 236.25 (SW)	60%	221.73 - 229.03	222.03 - 229.06
SM 02	213.75 - 236.25 (SW)	70%	224.44 - 231.95	224.39 - 231.53
SM 03 (ref.)	213.75 - 236.25 (SW)	100%	224.53 - 233.83	224.71 - 233.44
SM 05	213.75 - 236.25 (SW)	85%	223.87 - 232.91	224.03 - 232.64
SM 13	213.75 - 236.25 (SW)	60%	218.59 - 226.78	219.15 - 226.83
SM 17	213.75 - 236.25 (SW)	74%	224.72 - 233.99	224.94 - 233.45

## 5.2 | Downstream tower locations

A comparison between the predicted mean wind directions and the most frequent measured wind sectors at 57-m AGL on the met-towers (SM 09, 11, 12, 14, 15, 16, 18, and 19) located downstream of the main ridge is shown in Table 3. More than 60 % of all the samples on each met-tower fall within the SW wind sector which is consistent with the direction at the reference tower SM 03. The predicted wind directions from both RANS turbulence models at the locations of each met-tower are quite consistent. The predicted wind directions all fall into the most frequent wind sector without deviating too much (less than 4°) from the direction of the inflow (227°).

The comparison of the predicted mean wind speed and the conditionally averaged tower data at each met-tower located downstream of the main ridge is shown in Figure 20A. The predicted wind speeds at the met-towers SM 09, 14, 15, 16, 18, and 19 located relatively close to the main ridge are lower than the conditionally averaged tower data. This indicates that the real wind recovers faster than the simulated flow after passing through the lee side of the hill. The mean wind speeds predicted by both the  $k-\epsilon$  and SST  $k-\omega$  model are almost identical with very small differences no larger than 5%. A possible explanation for the small differences between  $k-\epsilon$  and SST  $k-\omega$  model results can be explained by the fact that none of these met-towers is located within the regions of boundary layer separation, which can be clearly observed in the contours of wind velocity components shown in Figure 15. We can only speculate about the reasons for the more systematic difference between the simulation results

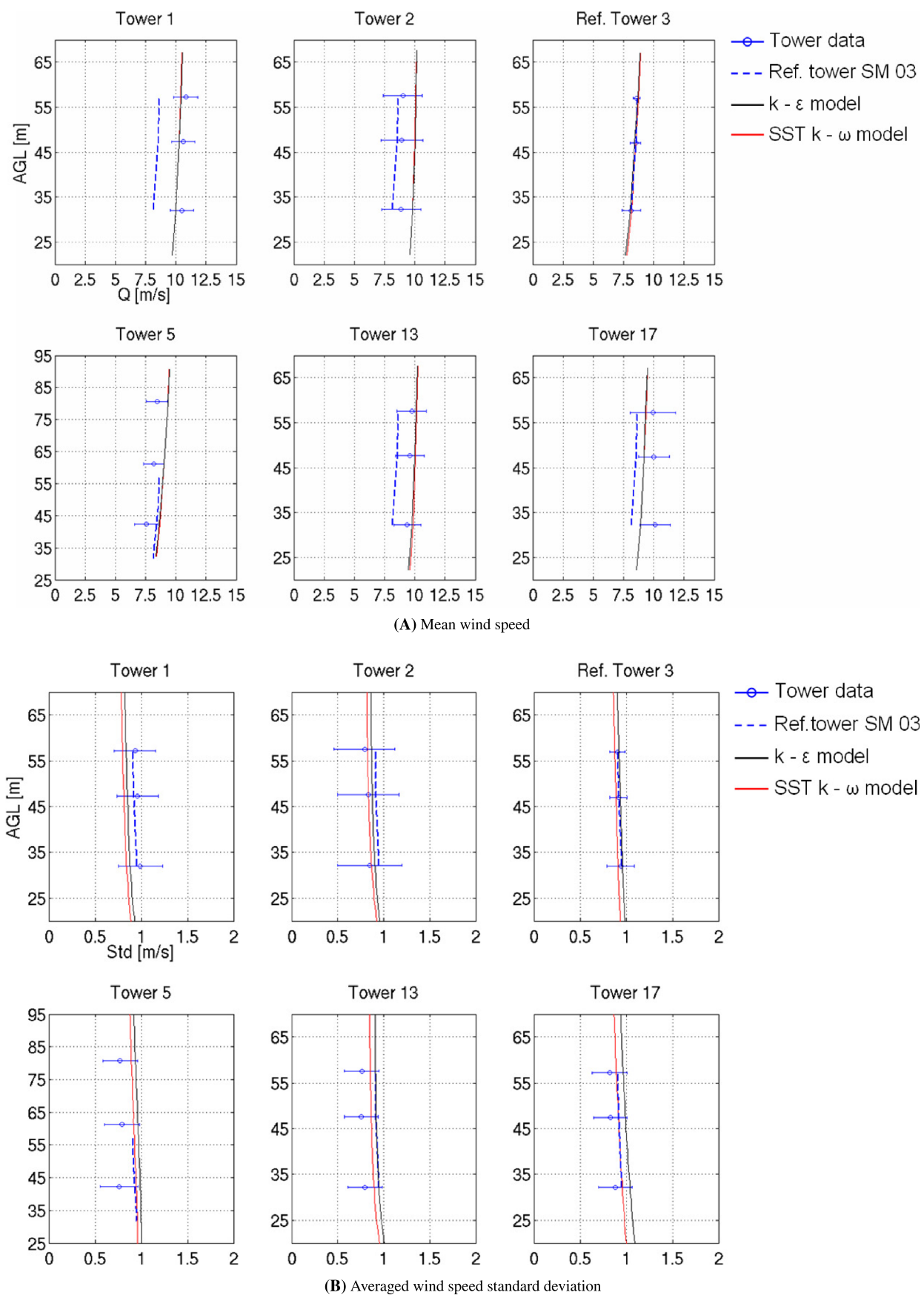


**FIGURE 19** Comparisons between the simulations and field measurement at met-towers located upstream of the main ridge [Colour figure can be viewed at [wileyonlinelibrary.com](http://wileyonlinelibrary.com)]

**TABLE 3** Comparison of the predicted wind direction ranges and the observed most frequent wind direction sectors at 57-m AGL on each met-tower located downstream of the main ridge

Met-tower	Tower Observations		RANS Simulated Wind Direction $\Phi_{sim}$ , °	
	Most Frequent Wind Sector, °	Frequency	$k-\epsilon$	SST $k-\omega$
SM 09	213.75 - 236.25 (SW)	80%	224.70 - 236.83	225.02 - 235.93
SM 11	213.75 - 236.25 (SW)	61%	223.80 - 233.97	223.76 - 233.55
SM 12	213.75 - 236.25 (SW)	70%	221.09 - 232.38	220.17 - 230.80
SM 14	213.75 - 236.25 (SW)	68%	222.88 - 233.85	223.60 - 233.77
SM 15	213.75 - 236.25 (SW)	85%	223.58 - 234.33	223.36 - 233.65
SM 16	213.75 - 236.25 (SW)	90%	215.40 - 229.33	215.22 - 228.59
SM 18	213.75 - 236.25 (SW)	85%	220.62 - 233.96	221.19 - 233.45
SM 19	213.75 - 236.25 (SW)	78%	223.89 - 235.16	223.72 - 233.92

from both RANS models and the conditional averaged tower data at towers SM 09, 14, 15, 16, 18, and 19. One possible explanation is that since the lee side of Miller hill is facing east it warms up earlier in the day thereby already causing locally unstable conditions and thus a better “mixed” boundary layer when conditions on the reference tower SM 03 are still close to neutral. This could explain the faster recovery of the measured wind speed compared with the simulation results. Another explanation might be that since both turbulence models are based on the linear eddy viscosity assumption they are not very well suited to predict flows with large extra strains such as occur in the “curved boundary layers” over the lee side of Miller hill. This latter hypothesis will be assessed in a future study using LES for the complex terrain ABL. As the flow streams over a relatively flat terrain to the locations of met-towers SM 11 and 12 (more than 5 km away from the main ridge), the turbulence models are better suited of capturing the mean flow features so that the agreement between predicted and measured wind speed profiles is better in this region.

The comparison of the predicted wind speed standard deviations and the tower data is shown in Figure 20B. The profiles of wind speed standard deviation predicted by the two RANS models show similar trends. However, the SST  $k-\omega$  model consistently predicts values between 3% to 10% lower than those of the  $k-\epsilon$  model. Overall, the simulated wind speed standard deviations agree well with the measured profiles at most of the tower locations. At met-towers located close to the foot of the Miller hill (SM 09, 18, and 19), the wind speed standard deviations are slightly under-predicted. It is worthwhile mentioning that clusters of trees are growing in some regions on the lee side of the hill around or upstream of these met-towers, which might increase the surface roughness locally. The increased surface roughness could help to explain the higher levels of wind speed standard deviation observed in the tower data. However, local vegetation information at the required resolution is not available at this point, and thus, such variations of  $z_0$  have not been considered in the simulations. This might be an interesting aspect of a future study.

### 5.3 | Comparisons of simulation results with conditional met tower data based on an alternative reference tower

Some differences between the simulation results and the tower data have been observed in the preceding discussion. These met-towers, including SM 02, 09, 16, and 18, are located in the regions either just upstream or downstream of the main ridge. To ensure that our findings are not sensitive to the choice of the reference tower, the conditional sampling process is performed based on a different reference tower and the tower data are again compared with the simulation results. If the conditional sampling process is robust and a reasonable reference tower is chosen, then the conditionally averaged wind statistics at all the met towers should not be very sensitive to the choice of the reference met-tower.

Since met-tower SM 05 is located relatively close to SM 03 and is surrounded by similar topographic features (a fairly flat plateau in the upstream region) as SM 03, it is reasonable to choose it as an alternative reference tower. Note that the data collection period on the met-tower SM 05 is around 6 years which is 2 years less than that on met-tower SM 03, so overall, we will have fewer samples. We apply the same conditions on SM 05 as we did on SM 03 (summer months,  $\bar{V} = 8.59 \text{ m/s} \pm 0.5 \text{ m/s}$  from  $227^\circ \pm 5^\circ$ ). There is a minor inconsistency in that these conditions are used for the cup anemometer data at AGL = 57 m on SM 03 and at AGL = 60 m on SM 05. We denote this conditional data set on SM 05 by  $R_{S,V}^{60m}$ , and we emphasize that the time stamps of  $R_{S,V}^{60m}$  do not need to coincide and with those from the SM 03 set  $R_{S,V}^{57m}$ . Since tower SM 05 has a cup anemometer installed at AGL = 80 m, the neutral stability threshold criterion as proposed in Wharton and Lundquist,<sup>40</sup>  $9\% \leq Tl_{Qcup} \leq 12\%$  can be applied directly at 80-m AGL (including the “two consecutive times” condition), and thus, the procedure does not depend on the choice for  $z_0=0.035\text{m}$ . Similar with the findings on SM 03, the majority of the samples identified as neutral on SM 05 occur during the few hours after sunrise and before sunset. We can also confirm that the wind shear criterion Wharton and Lundquist<sup>40</sup> on SM 05 is satisfied  $0.1 \leq \alpha_{SM05}=0.12 \leq 0.2$ . It should be emphasized that the samples in  $R_{S,V,N,\epsilon}^{60m}$  from SM 05 are almost

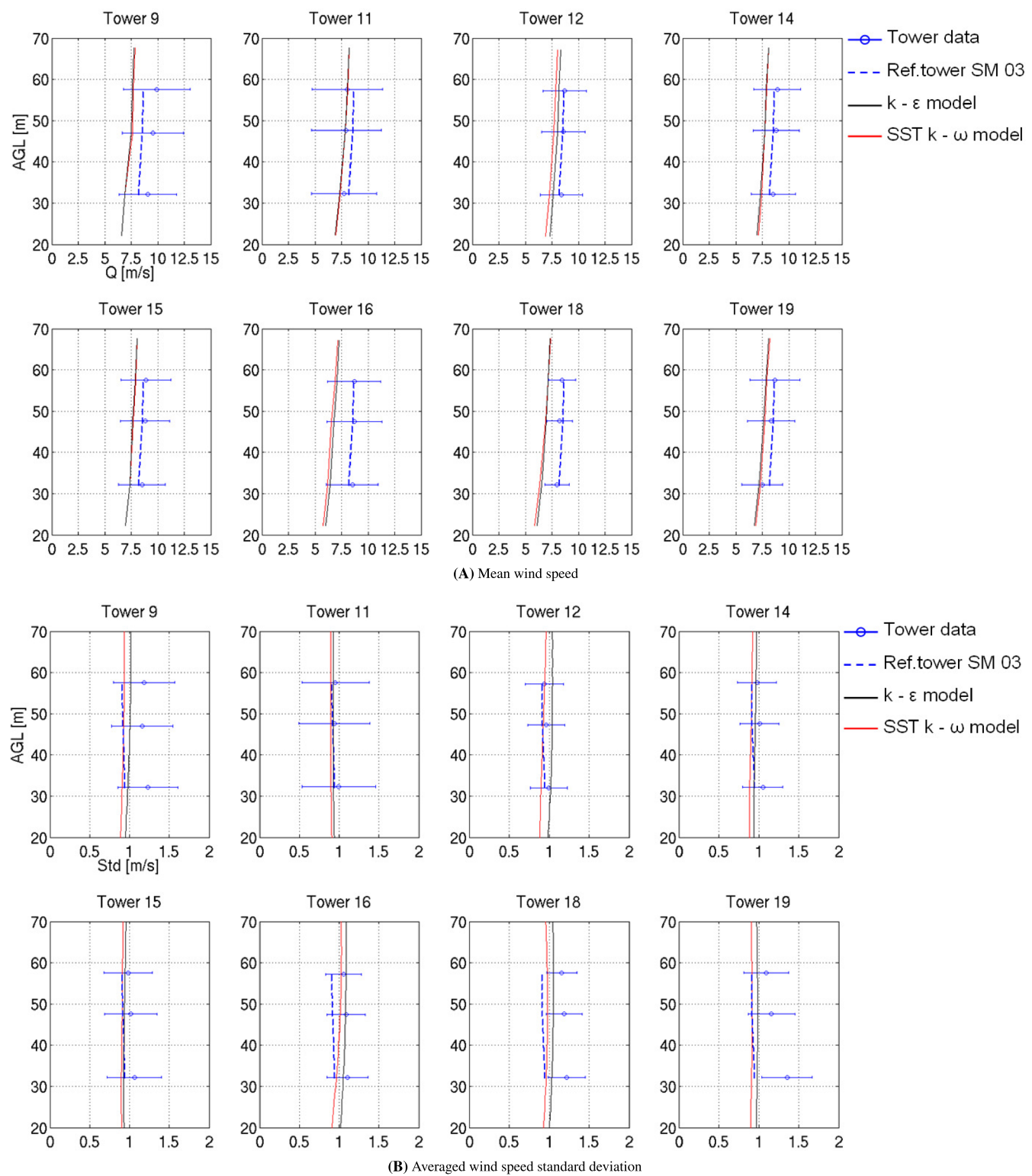


**FIGURE 20** Comparisons between the simulations and field measurement at met-towers located downstream the main ridge [Colour figure can be viewed at [wileyonlinelibrary.com](http://wileyonlinelibrary.com)]

completely independent from the samples  $R_{S,V,N,t}^{57m}$  of SM 03, and thus, independent conditional averages on all the other met-towers can be obtained.

The conditional averaged wind statistics of the “problematic” met-towers mentioned above are shown in Figure 21 based on reference tower SM 05. For comparison, the wind statistics based on the reference tower SM 03 and the simulation results using the  $k-\epsilon$  model are

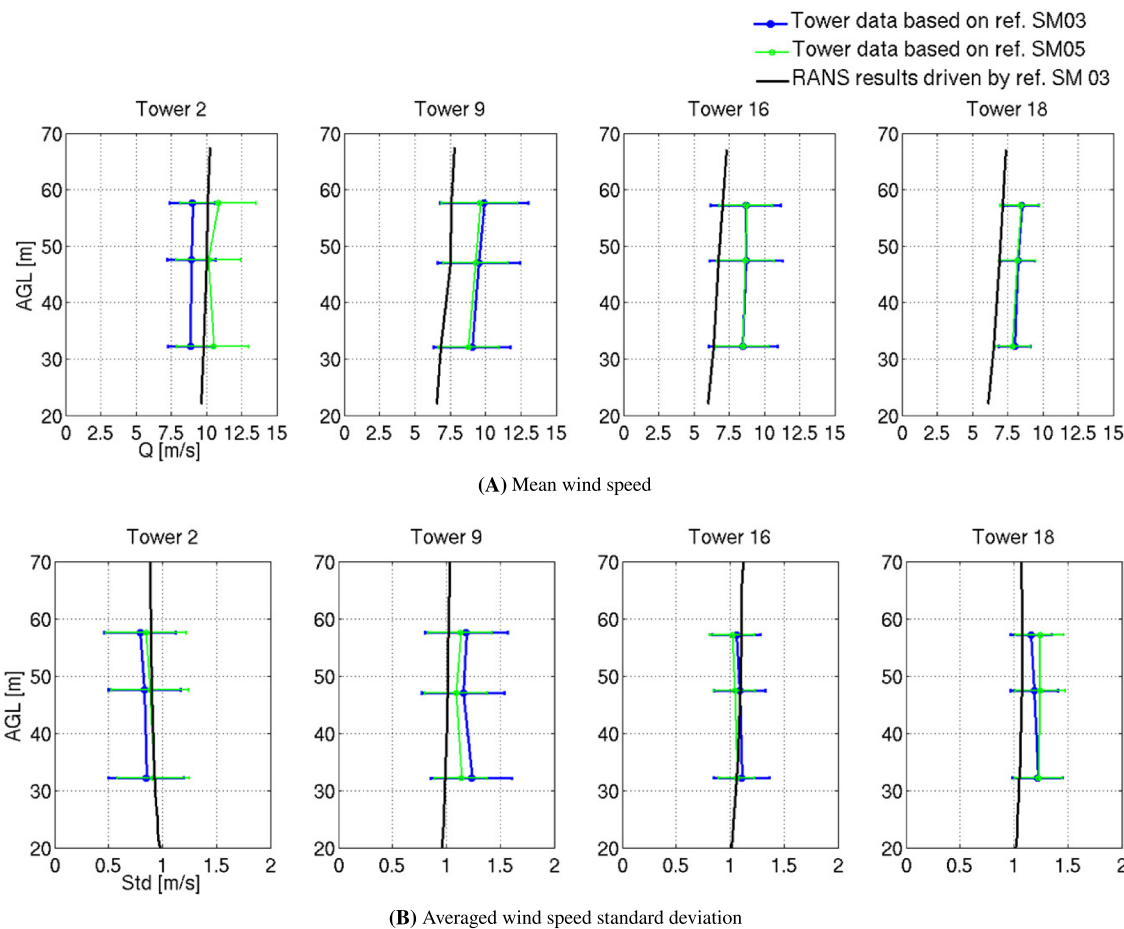


**FIGURE 21** The conditional averaged wind statistics on met-towers SM 02, 09, 16, and 18 obtained with SM 05 as the reference tower (RANS results from  $k-\epsilon$  model) [Colour figure can be viewed at [wileyonlinelibrary.com](http://wileyonlinelibrary.com)]

overlaid in each plot. Overall, the consistency between the statistics and even the uncertainties obtained with the two different reference towers is remarkable. The only larger difference is observed on tower SM 02, and this difference can easily be explained with the insufficient number of samples since tower SM 02 was removed 3 months after SM 05 has been installed. The consistency of the conditional wind statistics on all the other met towers (not shown) is comparable. This comparison demonstrates that the developed conditional sampling process is very robust and provides statistical results that are not very sensitive to the choice of the reference tower. Moreover, this also implies that the conclusions drawn from the comparison between the simulation results and the met tower statistics regarding the observed differences remain unchanged.

## 6 | SUMMARY AND CONCLUSIONS

This present work describes a complete process to perform micro-scale RANS simulations of the neutral ABL flow over a potential wind site in complex terrain including an attempt to validate the predictions with available met-tower data. The simulations are driven by conditional wind statistics obtained from a reference met-tower. A conditional sampling procedure for obtaining the near-neutral wind samples in the absence of multi-point temperature measurements is developed based on a criterion for the turbulence intensity at a prescribed above ground level. The conditional wind samples at the other met-towers are obtained according to the time stamps of the conditional data set of the reference tower. The conditional averaged wind speed and wind speed standard deviations as well as wind direction are calculated at all met-towers, which is used in comparisons with the simulation results. The conditional sampling approach provides robust wind statistics which are fairly independent of the choice of the reference tower.

The RANS simulations of the ABL flow are conducted using modified SOWFA solvers with the  $k-\epsilon$  and the SST  $k-\omega$  turbulence models. The driving inflow is generated through a two-stage iterative approach so that the measured wind statistics on the reference tower are reproduced in the simulations. New boundary conditions have been implemented to allow for entrainment through the top and lateral boundaries. Following a

suggestion by Richards and Hoxey,<sup>58</sup> a new discretization of the TKE production term  $P_k$  has been developed which involves averaging over the faces of a cell using a tighter stencil for the velocity gradients to mimic the discretization of the shear stress in the momentum equation as a Laplacian. The modification of  $P_k$  provides improved predictions of the mean wind speed and turbulent kinetic energy for both turbulence models in the flat precursor simulations. For the terrain simulations, the results at the met-tower observation heights are not sensitive to the discretization of  $P_k$ .

Qualitatively, the simulation results from the two turbulence models differ mostly in regions with strong elevation changes. The SST  $k-\omega$  model predicts more intense flow separation and recirculation compared to the  $k-\epsilon$  model in the near-surface regions on the lee side of the hill. The shear layers which are formed due to the flow separation and recirculation cause a large production of turbulent kinetic energy which is convected downstream and slowly weakened by turbulent transport and dissipation. It is somewhat unfortunate that none of the met-towers is located within the regions of possible flow separation to confirm the local flow feature predicted by the turbulence models.

The mean wind speed profiles predicted by the  $k-\epsilon$  and the SST  $k-\omega$  models at the locations of the met-towers are very similar and only slight differences of the predicted wind speed standard deviation profiles are observed. The simulation results predict the conditional averaged met-tower data for the direction, mean, and standard deviation of wind speed on most of the met-tower locations within the data uncertainty. Larger differences between the simulations and tower data are observed at the met-towers SM 02, 09, 16, and 18 which are located closer to the main ridge of the hill in a region of strong terrain variations. These differences could be attributed to the intrinsic weakness of the eddy viscosity based RANS turbulence models which are known to be less suitable for flows with extra strains such as in curved boundary layers. Another possible reason for the differences between simulations and measurements at those tower locations could be due to local changes of the atmospheric stability conditions, e.g., near the east facing slopes that warm up earlier in the day. The former hypothesis for the observed differences will be analyzed in a future study where we will use Large Eddy Simulation to predict the ABL over the complex terrain.

For a proposed wind farm site located in complex terrain with a prominent topographical feature (e.g., hill), it is confirmed by both simulations and measurements that wind turbines should be placed on the windward side of the hill approaching the peak, where the flow gets accelerated with lower levels of turbulent fluctuations (or turbulence intensity). For the region downstream of the hill, the wind turbines should be placed at a distance about four to five times of the relative hill height away from the ridge, where the levels of the mean and standard deviation of wind speed recover to the upstream values.

## ACKNOWLEDGEMENTS

This work has been funded by the US Department of Energy, Office of Science, Basic Energy Sciences, under award number DE-SC0012671. We would like to acknowledge the National Wind Technology Center (NWTC) of NREL for offering the open source SOWFA package. We also acknowledge the Power Company of Wyoming for providing the raw met-tower data on the CCSM wind site. We express great appreciation to NCAR-Wyoming Supercomputing Center (NWSC) for the support with high performance computational resources. We would also like to thank the reviewers whose insightful feedback has greatly improved this paper.

## ORCID

Yi Han  <https://orcid.org/0000-0001-5227-0385>

## REFERENCES

1. Wiser R, Lantz E, Mai T, et al. Wind vision: a new era for wind power in the United States. *Electr. J.* 2015;28(9):120-132.
2. Bailey BH, McDonald SL, Bernadett DW, Markus MJ, Elsholz KV. Wind resource assessment handbook: Fundamentals for conducting a successful monitoring program, National Renewable Energy Lab., Golden, CO (US); AWS Scientific, Inc; 1997.
3. Rodrigo JS, Arroyo RAC, Moriarty P, et al. Mesoscale to microscale wind farm flow modeling and evaluation. *WIREs Energy Environ.* 2017;6(e214). <https://doi.org/10.1002/wene.214>
4. Kirby AC, Brazell MJ, Yang Z, et al. Wind farm simulations using an overset hp-adaptive approach with blade-resolved turbine models. *The International Journal of High Performance Computing Applications.* 2019;33(5):897-923. <https://doi.org/10.1177/1094342019832960>
5. Vijayakumar G, Brasseur J, Lively AW, Jayaraman B, Craven B. Interaction of atmospheric turbulence with blade boundary layer dynamics on a 5MW wind turbine using blade-boundary-layer-resolved CFD with hybrid URANS-LENS. In 34th Wind Energy Symposium, AIAA SciTech Forum. San Diego, CA; 2016;521. <https://doi.org/10.2514/6.2016-0521>
6. Kirby AC, Hassanzadeh A, Mavriplis D, Naughton JW. Wind turbine wake dynamics analysis using a high-fidelity simulation framework with blade-resolved turbine models. In 2018 Wind Energy Symposium, AIAASciTech Forum, Kissimmee, Florida; 2018-0256. <https://doi.org/10.2514/6.2018-0256>
7. Spalart PR. Detached-eddy simulation. *Annu Rev Fluid Mech.* 2009;41:181-202.
8. Wang Y, Basu S, Manuel L. Coupled mesoscale-large-eddy modeling of realistic stable boundary layer turbulence. arXiv preprint arXiv:13072484; 2013.
9. Draxl C, Churchfield M, Mirocha J, et al. Coupling a mesoscale numerical weather prediction model with large-eddy simulation for realistic wind plant aerodynamics simulations (poster), National Renewable Energy Lab.(NREL), Golden, CO (United States); 2014.

10. Rodi W. Comparison of LES and RANS calculations of the flow around bluff bodies. *J Wind Eng Ind Aerodyn.* 1997;69(71):55-75.
11. Launder BE, Spalding DB. The numerical computation of turbulent flows. *Numerical prediction of flow, heat transfer, turbulence and combustion*; 1983 Jan 1 (pp. 96–116). Pergamon.
12. Hargreaves N. On the use of the k- $\epsilon$  model in commercial CFD software to model the neutral atmospheric boundary layer. *J Wind Eng Ind Aerodyn.* 2007;95(5):355-369.
13. Balogh M, Parente A, Benocci C. Rans simulation of ABL flow over complex terrains applying an enhanced k- $\epsilon$  model and wall function formulation: Implementation and comparison for fluent and openfoam. *J Wind Eng Ind Aerodyn.* 2012;104:360-368.
14. Menter FR. Performance of popular turbulence model for attached and separated adverse pressure gradient flows. *AIAA J.* 1992;30(8):2066-2072.
15. Menter F. Zonal two equation k- $\omega$  turbulence models for aerodynamic flows. In 23rd fluid dynamics, plasmadynamics, and lasers conference 1993 Jul 6 (p. 2906).
16. Menter FR. Two-equation eddy-viscosity turbulence models for engineering applications. *AIAA J.* 1994;32(8):1598-1605.
17. Wilcox DC. Reassessment of the scale-determining equation for advanced turbulence models. *AIAA J.* 1988;26(11):1299-1310.
18. Juretić F, Kozmar H. Computational modeling of the atmospheric boundary layer using various two-equation turbulence models. *Wind Struct.* 2014;19(6):687-708.
19. Hu P, Li Y, Han Y, Cai SCS, Xu X. Numerical simulations of the mean wind speeds and turbulence intensities over simplified gorges using the sst k- $\omega$  turbulence model. *Eng Appl Comput Fluid Mech.* 2016;10(1):359-372.
20. Yang Y, Xie Z, Gu M. Consistent inflow boundary conditions for modelling the neutral equilibrium atmospheric boundary layer for the sst k- $\omega$  model. *Wind Struct.* 2017;24(5):465-480.
21. Arya SPS, Shipman MS. An experimental investigation of flow and diffusion in the disturbed boundary layer over a ridge—I. Mean flow and turbulence structure. *Atmos Environ.* 1981;15(7):1173-1184.
22. Kim HG, Lee CM, Lim HC, Kyong NH. An experimental and numerical study on the flow over two-dimensional hills. *J Wind Eng Ind Aerodyn.* 1997;66(1):17-33.
23. Castro FA, Palma JMLM, Lopes AS. Simulation of the Askervein flow. Part 1: Reynolds averaged Navier-Stokes equations (k- $\epsilon$  turbulence model). *Bound-Lay Meteorol.* 2003;107(3):501-530.
24. Lopes AS, Palma JMLM, Castro FA. Simulation of the Askervein flow. Part 2: Large-eddy simulations. *Bound-Lay Meteorol.* 2007;125(1):85-108.
25. Bechmann A, Sørensen NN, Berg J, Mann J, Réthoré P-E. The Bolund experiment, Part II: blind comparison of microscale flow models. *Bound-Lay Meteorol.* 2011;141(2):245.
26. Putting wind to work for carbon county. Power Company of Wyoming <http://www.powercompanyofwyoming.com/index.shtml>; 2012.
27. Churchfield MJ, Vijayakumar G, Brasseur JG, Moriarty PJ. Wind energy-related atmospheric boundary layer large-eddy simulation using openfoam: Pre-print, National Renewable Energy Lab, Golden, CO (United States); 2010.
28. Churchfield MJ, Lee S, Michalakes J, Moriarty PJ. A numerical study of the effects of atmospheric and wake turbulence on wind turbine dynamics. *J Turbul.* 2012;13:14.
29. Churchfield M, Lee S, Moriarty P, Martinez L, Leonardi S, Vijayakumar G, Brasseur J. A large-eddy simulation of wind-plant aerodynamics. In 50th AIAA Aerospace Sciences Meeting including the New Horizons Forum and Aerospace Exposition. 2012 Jan 9 (p. 537).
30. Churchfield MJ, Sang L, Moriarty PJ. Adding complex terrain and stable atmospheric condition capability to the openfoam-based flow solver of the simulator for on/offshore wind farm applications (SOWFA), National Renewable Energy Lab.(NREL), Golden, CO (United States); 2013.
31. United States Department of Energy. 20% Wind Energy by 2030: Increasing Wind Energy's Contribution to U.S. Electric Supply. DOE/GO-102008-2567. July 2008. Available online:<https://www.nrel.gov/docs/fy08osti/41869.pdf>
32. Wind energy resource atlas - wind statistics by state: Prevailing wind direction table. Western Regional Climate Center. <https://wrcc.dri.edu/htmlfiles/westwinddir.html/WYOMING>; 2016.
33. Wind rose resources. Natural Resources Conservation Service (NRCS). <https://www.wcc.nrcs.usda.gov/climate/windrose.html>
34. Farr TG, Rosen PA, Caro E, et al. The shuttle radar topography mission. *Rev Geophys.* 2007;45(2).
35. Stull RB.. *An introduction to boundary layer meteorology*. Norwell, MA, USA: Kluwer Academic Publishers; 1988;ISBN 978-90-277-2796-5.
36. International Electromechanical Commission(IEC). Wind turbines part 12-1: power performance measurements of electricity producing wind turbines. Technical Report No. IEC 61400-12-1, 2005.
37. Welch M, Naughton J. Pre-possessing of the raw wind data in chokecherry and sierra madre wind site. Personal communication: naughton@uwyd.edu.
38. Talbot C, Bou-Zeid E, Smith J. Nested mesoscale large-eddy simulations with wrf: performance in real test cases. *J Hydrometeorol.* 2012;13(5):1421-1441.
39. Peña A, Hahmann AN. Atmospheric stability and turbulence fluxes at horns rev-an intercomparison of sonic, bulk and wrf model data. *Wind Energy.* 2012;15(5):717-731.
40. Wharton S, Lundquist JK. Assessing atmospheric stability and its impacts on rotor-disk wind characteristics at an onshore wind farm. *Wind Energy.* 2012;15(4):525-546.
41. Tielemans HW. Roughness estimation for wind-load simulation experiments. *J Wind Eng Ind Aerodyn.* 2003;91(9):1163-1173.
42. Frandsen S. Turbulence and turbulencegenerated structural loading in wind turbine clusters. Technical Report R-1188(EN), Roskilde, Denmark, Risø National Laboratory; 2007.

43. Gaultier G. Surface turbulence intensity as a predictor of extrapolated wind resource to the turbine hub height. *Renew Energy*. 2015;78:68-81.
44. Mortensen NG, Petersen EL. Influence of topographical input data on the accuracy of wind flow modelling in complex terrain. In 1997 European Wind Energy Conference 1998 (pp. 317–320). Irish Wind Energy Association.
45. Bowen AJ, Mortensen NG. Wasp prediction errors due to site orography. Risoe-R, No. 995(EN); 2004.
46. Lundquist JK. Assessing atmospheric stability at an onshore wind farm. In: Personal communication in International Conference on Future Technologies for Wind Energy. Boulder; 2017; CO, USA.
47. Harun Z, Monty JP, Mathis R, Marusic I. Pressure gradient effects on the large-scale structure of turbulent boundary layers. *J Fluid Mech*. 2013;715:477-498.
48. Lasher WC, Taulbee DB. On the computation of turbulent backstep flow. *Int J Heat Fluid Flow*. 1992;13(1):30-40.
49. Yan BW, Li QS, He YC, Chan PW. Rans simulation of neutral atmospheric boundary layer flows over complex terrain by proper imposition of boundary conditions and modification on the k- $\epsilon$  model. *Environ Fluid Mech*. 2016;16(1):1-23.
50. Kim HG, Patel VC. Test of turbulence models for wind flow over terrain with separation and recirculation. *Bound-Lay Meteorol*. 2000;94(1):5-21.
51. Pope SB. *Turbulent flows*. Cambridge: Cambridge university press; 2000.
52. Boussinesq J. Théorie de l'écoulement tourbillant. *Mém prés Acad Sci*. 1877;XXIII:46.
53. Menter FR, Kuntz M, Langtry R. Ten years of industrial experience with the sst turbulence model. *Turbul heat mass trans*. 2003;4(1):625-632.
54. Chan PW. Measurement of turbulence intensity profile by a mini-sodar. *Meteorol Appl J Forecast Practical Appl Training Tech Model*. 2008;15(2):249-258.
55. Thompson JF, Warsi ZUA, Mastin CW. *Numerical grid generation: foundations and applications*, (Vol. 45). Amsterdam: North-holland; 1985.
56. Han Y, Stoellinger M, Naughton J. Large eddy simulation for atmospheric boundary layer flow over flat and complex terrains. *J Phys Conf Ser*. 2016;753(3):032044.
57. Han Y, Stoellinger M. Large eddy simulation of atmospheric boundary layer flows over complex terrain with varying stability conditions. In: 35th Wind Energy Symposium, AIAA SciTech Forum, Grapevine, Texas, USA. 2017;1161. <https://doi.org/10.2514/6.2017-1161>
58. Richards PJ, Hoxey RP. Appropriate boundary conditions for computational wind engineering models using the k- $\epsilon$  turbulence model. *J Wind Eng Ind Aerodyn*. 1993;46:145-153.
59. Liu F, Hakan N. A thorough description of how wall functions are implemented in openfoam. In: Proceedings of CFD with OpenSource Software; 2016. [http://www.tfd.chalmers.se/~hani/kurser/OS\\_CFD\\_2016](http://www.tfd.chalmers.se/~hani/kurser/OS_CFD_2016)
60. Rhee CM, Chow WL. Numerical study of the turbulent flow past an airfoil with trailing edge separation. *AIAA J*. 1983;21(11):1525-1532.
61. Moukalled F, Mangani L, Darwish M, et al. The finite volume method in computational fluid dynamics. *An advanced introduction with OpenFoam® and Matlab®*. Springer International Publishing Switzerland. 2016.
62. Richards PJ, Norris SE. Appropriate boundary conditions for computational wind engineering models revisited. *J Wind Eng Ind Aerodyn*. 2011;99(4):257-266.
63. Holzmann T. *Mathematics, numerics, derivations and openfoam*. Leoben, forth eidition: Holzmann CFD; 2017. <http://www.holzmann-cfd.de>
64. Issa RI. Solution of the implicitly discretised fluid flow equations by operator-splitting. *J Comput Phys*. 1986;62(1):40-65.
65. Patankar SV, Spalding DB. A calculation procedure for heat, mass and momentum transfer in three-dimensional parabolic flows. *Numerical prediction of flow, heat transfer, turbulence and combustion*; 1983 Jan 1 (pp. 54–73). Pergamon.
66. Chevalier C, Pellegrini F. Pt-scotch: A tool for efficient parallel graph ordering. *Parallel comput*. 2008;34(6-8):318-331.
67. Slater W. Slater. Examining spatial (grid) convergence. <https://www.grc.nasa.gov/www/wind/valid/tutorial/spatconv.html>, Accessed July 17, 2008.

**How to cite this article:** Han Y, Stoellinger MK. RANS simulations of neutral atmospheric boundary layer flow over complex terrain with comparisons to field measurements. *Wind Energy*. 2020;23:91–119. <https://doi.org/10.1002/we.2412>